Master Thesis, Department of Geosciences

Heat Flux Modeling on Debris-Covered Glaciers

Jordan Robert Mertes

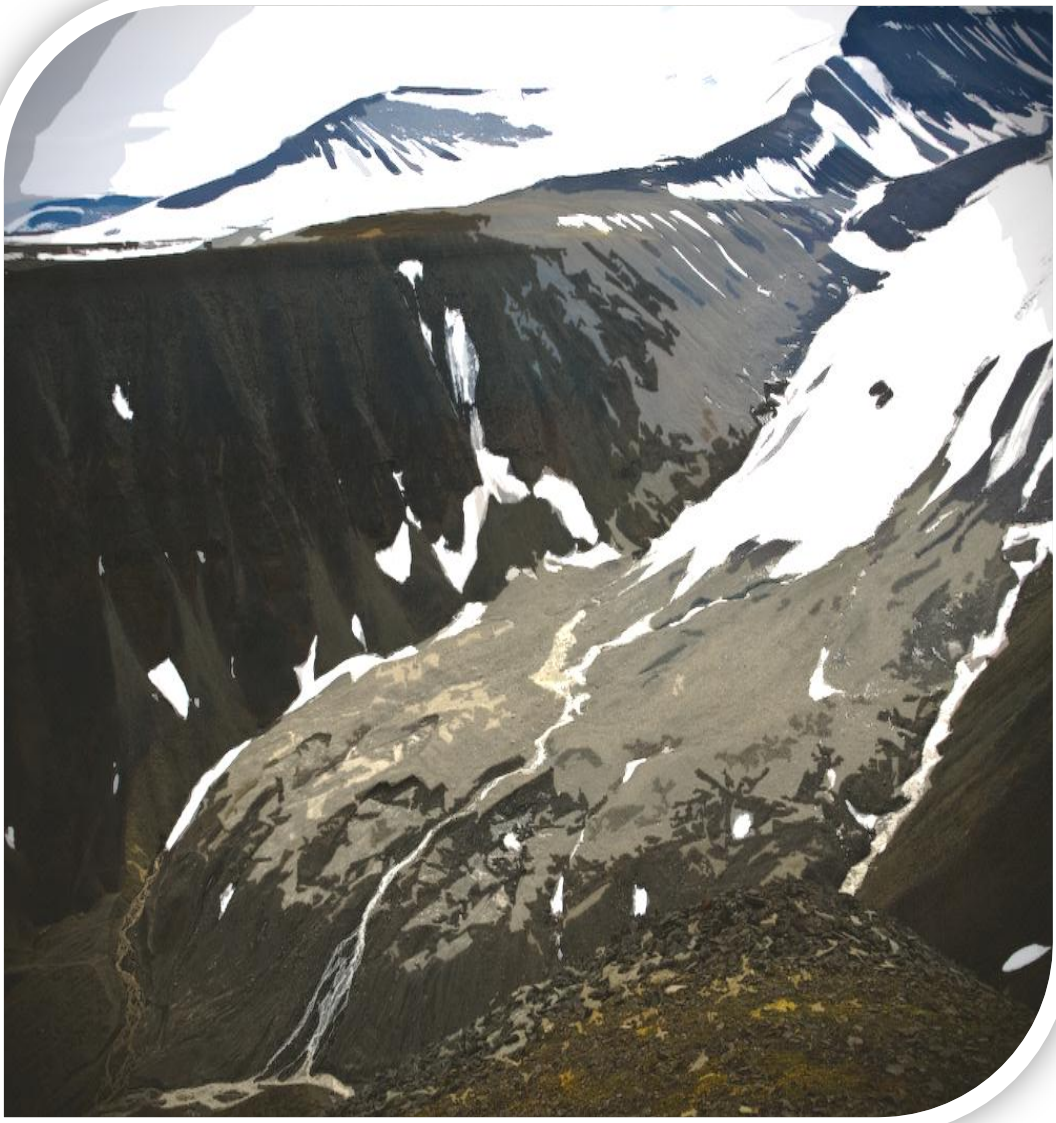

UNIVERSITY OF OSLO

FACULTY OF MATHEMATICS AND NATURAL SCIENCES

Heat Flux Modeling on Debris-Covered Glaciers

Jordan Robert Mertes

Masters of Science Thesis in Geoscience
Discipline: Physical Geography
Department of Geosciences
Faculty of Mathematics and Natural Sciences

UNIVERSITY OF OSLO
UNIVERSITY CENTRE IN SVALBARD

10 June 2011

Supervisor: Professor Ole Humlum, Department of Geosciences, University of Oslo

Supervisor: Professor Doug I. Benn, Department of Geology, University Centre on Svalbard

Heat Flux Modeling on Debris-covered Glaciers. Jordan Robert Mertes

Cover photo of Longyearbreen, Svalbard by Jordan Mertes, August 2009

This examination work is published online in DUO - Digital Publications at the University

http://www.duo.uio.no

It is also cataloged in BIBSYS (http://www.bibsys.no/)

Preface

First and foremost I would like to thank my family, friends and colleagues for being supportive of my academic ventures and for putting up with me being in the middle of the arctic for so long… even though I plan to stay longer. A special thanks to Sarah Thompson for never losing faith in me when I did so often.

Getting to study at UiO and UNIS with all the great professors such as Doug Benn, Ole Humlum, Hanne Christiansen, Bernd Etzelmüller and the numerous lecturers from abroad has been a highlight of my life. I could not have done this work without the help and advice I have gotten from all of the aforementioned especially Doug, Ole and Hanne. They have put up with my constant bombardment of questions for three years now and I've never been turned away. Each has helped me in their own way and I am very grateful for the advice, the insight, the knowledge gained and the encouragement given. A special thanks to Doug for the evenings of guitars and whiskey, Hanne for the job opportunities and academic guidance and Ole for the intriguing conversations and guided road trip through southern Norway, one of the best tours ever.

I would also like to thank Nick Hulton and Ian Rutt for helping me in the beginning when I was first setting out to develop my model. Even from thousands of miles away they were still more than happy to offer whatever help they could. I look forward to working with them more in the future if at all possible.

It is also imperative that I thank Prof. Gerald Recktenwald, of Portland State University, a man I have yet to meet face to face yet was always helpful when I was trying to build my model off an expansion of his simple model. It took many emails and many pages of paper to work through the equations but I finally got it and it wouldn't have been without his advice.

I owe a huge thank you to the Norwegian American Foundation (NORAM) for choosing me as a recipient for the Marshall Scholarship for 2 years running. This was crucial for my being here. I have to thank Tove Lain Knudsen, NORAM's director of scholarships for all the support and the numerous lunches whenever I was in Oslo.

A special thanks to the staff of UNIS for the work they do running UNIS. To Berit Jakobsen, a huge tusen takk for finding those hard to find papers and for being the only librarian I know who likes to play Jimi Hendrix IN the library.

To all my friends who have come and gone who had to put up with me working so much I say thanks for the good times, the beach, the øl, the pølse the café, the sauna, the fun and the music.

Abstract

A one-dimensional heat flux model has been developed in this study to analyze changes in heat propagation within debris cover on a glacier and the subsequent melt. The model can accept data collected *in situ* for calculations of real modeled melt, and also synthetic data based on simple wave forms and debris physical characteristics. The model is based on the Crank-Nicolson finite difference method of solving the one-dimensional heat equation. It has been written and implemented using MATLAB 2007b. A GUI has also been developed to allow for quick visualization and model adjustment. Numerous hypothetical runs have been performed to test the limitations of the model and to determine the accuracy and performance of the model.

The model has been used to study what differences arise when using the melt calculation method of assuming an average daily linear thermal gradient versus using a physically based model. From this it has been shown that under stable atmospheric conditions and a relatively thick (~>0.5m) debris layer, the linear method does produce results similar to the full physical model. However, during times of unstable atmospheric conditions, errors do arise as the internal heat storage begins to fluctuate rapidly. If using the linear method on thinner (~<0.5m) debris layers the errors grow in response to the underestimation of internal temperatures.

Using the model to analyze the changes in heat flux with varying debris thicknesses, a relationship between the two has been found, such that the linearity of the temperature profile is inversely related to the debris thickness. From this, a secondary relationship has also been found where the magnitude of the thermal gradient is also inversely related to the debris thickness. A comparison of calculated melt based on the assumption of a linear thermal gradient with that of the actual model shows a decreasing error with depth up to ~0.6m. It has been found that with an increasing debris thickness two things happen which decrease the error between the two methods. Firstly the magnitude of the modeled thermal gradient, at or near the surface, has been shown to decrease by almost a factor of 4 in this case, reducing the error between the two methods within this region of the debris. Secondly, the values for

modeled thermal conductivity at the debris-ice interface approach zero, thereby reducing the error between the two calculated melts in the lower regions as the debris thickens.

The model has also been used in an attempt to replicate results from a previous laboratory study performed by Reznichenko et al. (2010) where under stable conditions in a lab setting, melt was calculated under debris layers of varying thicknesses. The results of the model have been used as a verification of the accuracy of the model.

Using data from the 2010 melt season from Longyearbreen, melt calculations have been made using both the modeled and the linear thermal gradient method producing values of 0.54m and 0.47m respectively. A correction has been made to the melt calculated using the linear thermal gradient based on an analysis of the differences between the two gradients and a correlation with daily average surface temperatures. By applying this correction equation the final R^2 between the melt values was increased to 0.98.

An Østrem curve has also been created using the model and varying the debris thickness by sub-centimeter increments. Based on the model's performance tests and ability to produce similar melt results as laboratory results, the Østrem curve is believed to be more accurate in its general shape rather than its magnitude. The model has also been used to study the effects of measuring melt below varying debris thicknesses during shorter time periods throughout the melt season and how this subsequently changes the resulting Østrem curve. Differences on the order of ~0.5m have been found using 10 day periods during the mid-beginning melt season, mid-peak and mid-end of the melt season.

Table of Contents

List of Document Figures

List of Document Diagrams

List of Document Tables

1 Introduction and Thesis Aims

1.1 Debris-covered Glaciers

Debris-covered glaciers are glaciers that have an extensive layer of mainly unconsolidated material located in the ablation zone, in most cases covering the terminus. The buildup of this debris layer causes the glacier to undergo a change not only in appearance but also in its dynamic response to atmospheric influences. While much is already known about the ways in which a clean-ice glacier responds to changes in climatic factors, with the introduction of a debris layer comes a change in the system, thereby creating a need for a change in the models used for predicting such responses as melt.

1.1.1 Mechanisms of Debris Cover Formation

Two of the main mechanisms in which debris may accumulate on glaciers can be attributed to specific location types. There is the periglacial mechanism which involves sediment being entrained both supraglacially from slope degradation processes (e.g. frost shattering and avalanching) and subglacially (e.g. basal freeze on). This material is transported down glacier through regular flow and may be deposited on the surface through means of surging and thrusting of the subglacial material upwards or by stagnation and ablation where, as the surface lowers the entrained debris melts out and builds a layer over time. In areas of high relief, such as the Himalaya Mountains, debris is mainly transported to the glacier surface by avalanche activity.

1.1.2 Regional and Climatic Occurrence

Debris-covered glaciers can be found on nearly every continent aside from Africa. The glaciers of Kilimanjaro and Mt. Kenya do not appear to have any surface debris (Google Earth). On Mt. Kenya however, studies have shown aeolian sediments (i.e. windblown dust, ash, insects etc…) have been deposited on the surface and also become entrained into the ice and subsequently form banded layers (Charnley 1959). These thinner layers of dust sometimes

have more of an effect on melt than that of a thicker layer. The Himalaya Mountains contain some of the largest and longest debris covered glaciers in the world. On some glaciers it is possible to have sandy soil layers developing if the debris has been in existence for a long enough length of time.

On the Svalbard Archipelago the presence of debris cover on glaciers occurs on a smaller scale. Many Svalbard glaciers only show debris cover in the very end of the terminus regions. The debris is mainly from entrained materials melting out during the ablations period or from avalanches.

1.2 Debris Layer Effects on Melt and Mass Balance

The two main effects a debris layer has on a glacial system is changing the surface albedo and insulating the ice from heat from the atmosphere. Dry snow is known to have a high albedo (~ .80-.97), clean ice a moderate albedo (~.34-.51) and debris-covered ice a low albedo (~.10-.15) (Cuffey and Paterson 2010). The debris layer absorbs ~70-80% more solar radiation than dry snow, and ~20-40% more than clean ice. If the debris layer is below the critical thickness (i.e. thickness where the amount of energy received at ice surface is equal to a clean ice surface) (Østrem 1959) then ice ablation is increased. However, as the debris layer thickens past the critical thickness it begins to act as an insulator, and the amount of heat that is conducted through to the ice surface is lessened and the melt decreases (Nakawo and Rana 1999, Conway and Rasmussen 2000, Reznichenko et al. 2010). It is also important to point out the effects a debris layer has on ablation across the whole debris-covered area. Since the debris cover is not of a uniform thickness, differential ablation generally occurs causing high and low points on the surface (Nicholson 2004). Though the majority of the surface may be continuously covered, at locations of cracking or high slope angle, the debris may open up or slide off allowing heat flux to melt the underlying ice (Benn et al. 2001). This can lead to the formation of supraglacial lakes and potentially glacial lake outburst floods (GLOFs) (Cenderelli and Wohl 2001, Dortch et al. 2011).

1.3 Importance of Debris Covered Glaciers

Aside from the importance of debris-covered glaciers as an area of growing scientific research, their most important aspects come from their impact on civilization. Many towns and villages located near or downstream from glaciers depend on them as a source of water and in numerous cases even power. In some instances the glaciers may develop hazardous moraine dammed lakes which, if catastrophically released (through tectonic activity, rock falls, calving induced pressure waves or general moraine instability) may destroy villages and installations downstream. Since many of the populations that depend on glaciers for water and or power are located in remote areas, a catastrophic event such as a GLOF can cause changes that will be felt for many years afterwards.

1.3.1 Water Resource Management and Prediction

Melt modeling has its many difficulties. One of the main problems associated with modeling the surface heat flux is gathering the data needed to run an accurate model. Some have proposed "simple" models which still require numerous atmospheric inputs (Nakawo and Takahashi 1982, Braithwaite and Olesen 1990) while others gather just a few important atmospheric data and use empirically derived equations to calculate the other parameters. Finding a way to model sub-debris melt both accurately and with the least amount of effort is important for mountain communities. Coming up with a simple solution, which they themselves could do, would help them to be able to predict the annual amount of melt for use as potable water, irrigation and even hydropower (e.g. Thame Hydropower Plant, Khumbu, Nepal). Without this water these communities cannot thrive.

1.3.2 Glacial Lake Outburst Floods (GLOFs)

Moraine dammed lakes can be observed in the terminus and even lateral regions of numerous glaciers throughout the world. As a debris covered glacier ablates, the areas with a thick debris cover melt at a slower rate than those areas of clean ice. This may cause a frontal topographic high point which can dam any melt water that is produced. In many cases the surface lowers leaving the surrounding moraines at a higher elevation around the ablation zone. If there is no spillway to allow melt water to drain, the moraines act as a dam. If the lake grows large enough

it may burst through the moraine causing a GLOF to be released. Being able to predict heat flux and melt would allow scientists to monitor glaciers that may topographically have the potential to form moraine dammed lakes if the melt begins to rapidly increase.

1.4 Development of Heat Flux Models

For modeling how heat flows from the surface through a debris layer of varying geometries and physical characteristics a model has been developed using the Crank-Nicolson finite difference method of solving the one dimensional heat equation. The model is a build off of demoCN.m, a simple one dimensional heat model, using Dirichlet boundary conditions, created by Prof. Gerald Recktenwald of Portland State University. The model has been built to be more robust and accept numerous different values. The purpose of developing such a model is to compare the differences in calculated melt using a daily average linear melt model as used in Nicolson and Benn (2006) against the calculated melts from a physically based model as developed by Recktenwald (2011a). The model has also been implemented into a GUI allowing for ease of use and quick visual results. Different hypothetical tests were run on the model and finally it has been applied to a real world situation and compared to data gathered from Longyearbreen during the melt season of 2010.

1.5 Thesis Aims

The aims of this thesis are to firstly develop a fully functional one-dimensional heat flux model that can be used not only to simulate heat flux through an imaginary three layer system of atmosphere-debris-ice but to also accept field data on energy balance components and to predict the amount of heat flux at a specific location. Another aim of this study is to use the model to look at how the thermal gradients change with varying debris thicknesses and what affects this has on calculated melt found by using the linear thermal gradient method. The third aim of this study is to use the model in an attempt to replicate experimental laboratory results from Reznichenko et al. (2010) pertaining to the effects of debris layer thicknesses and diurnal cycle amplitude and length have on heat flux and melt. The final aim of this study is to use atmospheric and ground temperature data collected during the 2010 melt season on

Longyearbreen to force the model and calculate a season melt and an Østrem curve for Longyearbreen.

By validating the model's ability to reproduce melt through means of modeling the physical heat flux is important in that by having an accurate model allows for the testing of the limitations of using the linear gradient method. This method, which is commonly used on debris covered glaciers, is an oversimplification of heat flux and works under certain assumptions. By determining under what conditions the method produces the least amount of error will allow for scientists to make a better decision on whether or not to use a full physical model or the linear gradient method. The model will also be used to model melt for the Longyearbreen study site during the melt season of 2010.

1.6 Thesis Structure

Section 2: A brief introduction to the glacier system and characteristics is given along with an explanation of glacial mass balance and how debris layers affect mass balance.

Section 3: An in depth derivation of the energy balance equation and its different variables is given as well as a discussion of how the input of each is affected by the presence of debris cover. The equations implemented into the one-dimensional heat flux model are given in this section.

Section 4: The development of the one dimensional heat flux model and how it is implemented is presented. Derivations from the heat equation using finite approximations are discussed and the equations and mathematics behind the model are presented. The latter part of this section discusses the testing of the initial model and its potential errors.

Section 5: An introduction to the model GUI that was developed is given along with the results of modeled runs looking at the changes in melt, thermal gradients and debris relaxation times is given. The results from recreating the laboratory experiments of Reznichenko et al. (Reznichenko et al. 2010) are also presented.

Section 6: The study site background for Longyearbreen is presented along with information on the instruments used for data collection. Instrument performance data are also given. The application of the model to the field data is discussed. Model runs were performed using both surface energy data from a weather station, and also from surface temperatures recorded during the field season.

Section 7: A discussion of the results from all tests and runs is presented along with conclusions of the model's performance and future application possibilities.

2 The Influence of Debris Cover on Glacier Mass Balance

2.1 What is Mass Balance

Glaciers are mainly made up of two areas, the accumulation area where mass is accumulated and the ablation area where mass is lost. Between these two areas there are numerous other "zones". Working from the accumulation area to the ablation area, these zones are as follows (Cuffey and Paterson 2010):

Accumulation Area

1. Percolation Zone (Melt water percolates into the snowpack)
2. Wet Snow Zone (Snow in this zone is heavily saturated with water)
3. Superimposed-ice Zone (Melt water from the wet snow zone refreezes here, creating an annual layer of superimposed-ice)

Ablation Area

The defining line separating the accumulation area from the ablation area is commonly referred to as the equilibrium line, and is given a value of the elevation at which it occurs, hence the acronym "ELA" or Equilibrium Line Altitude. At this defining line the annual accumulation of snow is exactly equal to the annual ablation. Determining the ELA was initially done by setting up a series of ablation stakes along a longitudinal transect of the glacier. These stakes are set into the ice allowing measurements to be made on the amount of accumulation and ablation along the glacier length. From these data it is possible to determine the elevation where the balance is in equilibrium.

The measurements are generally made over a specific period of time (e.g. hydrologic year, 1 year, on specific dates). By looking at the winter gain and the summer loss one can calculate the mass balance as follows,

$$b_n = b_w + b_s \quad where\ b_s < 0 \qquad 2.1.$$

Along with stake readings it is standard procedure to take depth soundings and measure snow density at the point sites (Kaser et al. 2003). Once all the data have been gathered, to get an accurate representation of the whole glacier, the accumulation or ablation at specific altitude intervals can be calculated using topographic maps to yield a mass balance in terms of melt water equivalents (m.w.e) or the amount of water produced from the melting within the area between two altitude intervals. The number of stakes used is left up to the researcher. However due to the difficulty in getting the measurements, the number of stakes should generally decrease with the size of the glacier and the error should remain negligible as found during an ongoing study of mass balance of ~50 glaciers in Norway (Andreassen et al. 2005).

The altitude of the ELA is not a constant; it is the average across the glacier as the position of the ELA may change due to glacier morphology or surrounding topography. Glaciers located in high relief mountain regions may have ELAs that vary greatly due to topographic shading of certain areas or from redistribution of snow through predominant winds. It is possible to study a glacier's response to a changing climate through monitoring the ELA of a glacier and its annual mass balance. By doing this one can extrapolate where the steady state ELA (ELA where zero annual mass balance occurs) would occur and how the mass balance will increase or decrease in response to a warming or cooling climate (Benn and Lehmkuhl 2000). In more recent years, through the use of aerial photography and remote sensing data it has become possible to visually see the zone of the ELA on many glaciers as a distinct change up glacier from ice to snow. A line along this border should not always be considered a precise ELA as there are areas below this line which may be saturated snow (i.e. wet snow zone) where melt from the surface snow has percolated down through the snowpack and either refreezes to form a layer of superimposed ice or may runoff. It may be difficult from a distance to distinguish the superimposed ice from the bare ice. There are numerous methods to determine past ELAs through the use of geomorphology. One simple way in particular is to find the high point, or beginning of moraines within the catchment. This of course assumes that englacial debris is released at the ELA. This however may or may not be the case as debris may not melt out until it is lower than the ELA (Benn and Lehmkuhl 2000).

2.2 Global Mass Balance Changes

During the last ~50 years some countries around the world have been monitoring glaciers within their own borders and also more remote unpopulated areas. The methods used range from the traditional method of ablation stakes to topographic analysis of maps or even using hydrologic data (Tangborn et al. 1971, Andreassen 1999, Hagen et al. 1999, Jansson 1999). With the increase in availability of remotely sensed data, the traditional methods have been upgraded so to speak. Using satellite derived digital elevation models (DEMs) or satellite laser altimetry, allows the collection of highly accurate surface elevation data. In the last few years even the use of gravitational anomaly data has been used to detect mass changes (Luthcke et al. 2008).

Norway has been conducting mass balance measurements on local glaciers since 1949 (i.e. Storbreen) and in total, in the year 2005, had 517 glacier-years of data (Andreassen et al. 2005). Certain glaciers in Svalbard have had mass balance measurements done on them since the 1950s (Hagen and Liestøl 1990, Hagen et al. 1999, Hagen et al. 2003a, Hagen et al. 2003b). In more recent years, through the use of remote sensing data (i.e. ICESat), elevation changes of Svalbard glaciers have been measured and compared to surface elevations from older topographic maps (Nuth et al. 2010). In Sweden there is also has a long history of mass balance measurements including those made on Storglaciären since 1946 and also some earlier photographic estimates from the late 19th century (Holmlund 1987).

Elsewhere throughout the world, during the last few decades, there has been an increase in the number of glaciers being monitored and a push for some underdeveloped countries to begin monitoring benchmark glaciers in order to get a clearer picture on what is happening in their regions. By combining all the mass balance data together it's possible to get a better understanding of how glaciers are changing and what their climatic environments are. In the IPCC report of 2007 it was stated that many glaciers in the Himalaya may be gone by ~2035 (Parry et al. 2007) . This statement was later retracted by the IPCC but caused major unrest in the worldwide population. Recent findings have shown that the response to climatic changes, especially in the Himalaya, is regionally dependent and some glaciers are advancing, some are

retreating and others are holding fast (Shroder et al. 2008). In Svalbard glacial monitoring is important, as global climate change models have shown the arctic areas are the areas that will experience the most warming if trends continue as they are.

2.3 Effects of Debris Cover

One of the most prominent effects of debris cover on glaciers is its ability to shield the glacier from incoming atmospheric heat sources. This causes the debris covered area to respond more slowly to climatic changes. In many regions where there has been a noted annual warming, glaciers with debris covered ablation zones appear to be much less affected by the warming. While the regional ELA may be increasing, those glaciers with debris cover are able to endure the increased warming in their lower regions.

For glaciers with a moderate layer of debris, changes due to warming may be manifested in the form of stagnation and down wasting (surface lowering) as opposed to retreat. Many debris covered glaciers throughout the world have been noted to be down wasting and in many cases are developing undulating surface topography due to differential melting. In some of the more extreme cases this down wasting has led to the formation of supraglacial lakes (Figure 1).

Figure 1: Supraglacial lakes forming on the Ngozumpa glacier, Nepal Himalaya.

The presence of supraglacial lakes, in some cases, counteracts the insulating effects of debris and causes an increase in melt, specifically in the shore line areas, many of which may have exposed ice faces. Some potential causes of this increased melt may also be attributed to the

dumping of warm supraglacial debris into the newly developed lakes. The amount of heat transferred from the debris to the water may be enough to keep it at a warmer temperature than normal, causing ice face undercutting, possible calving and shore line retreat.

As a debris covered glacier does down waste or retreat the surrounding moraine may become a dam to any melt water produced during the ablation season. These moraine dams have the potential to entrap supraglacial lakes as they become larger. If this occurs and the lake reaches to the bottom of the glacier and to the terminal moraine then the forefront of the glacier becomes a calving front, and through more increased melting the lake may grow to a hazardous size. In the case where these moraine dammed lakes are not drained there is a heightened risk of a GLOF.

3 The Influence of Debris Cover on Glacier Ablation

Solar radiation enters the atmosphere with a mean annual magnitude of 1367W/m^2, also known as the solar constant (Cuffey and Paterson 2010). A portion of this energy is reflected back into space and some is absorbed by atmospheric aerosols. The remaining energy is transmitted to the Earth's surface, where depending on the surface albedo, a portion will be reflected back to the atmosphere and the rest is absorbed by the Earth. The absorption of this energy contributes to the Earth's surface temperature and is reemitted in the form of longwave thermal radiation. Thermal radiation may also be emitted by the atmosphere downwards towards the Earth's surface.

Other fluxes come from the temperature differences between the surface and the air above it (i.e. sensible heat), as well as from precipitation and energy released or absorbed during phase changes (i.e. condensation, vaporization or sublimation). Solar radiation has been shown to account for up to 75-99% of the available energy at the surface in mid to high latitude environments (Arnold et al. 2006). The energy budget equation sums all of the incoming (i.e. directed towards the surface, ↓) and outgoing (i.e. directed away from the surface, ↑) energy fluxes and the total dictates whether warming or cooling of the surface will occur.

This section develops the essential equations used in the model for this study. Values used in the model, when applied to field data from the study site, are given during explanation.

3.1 Energy Budget Equation

The components of the energy budget equation (Equation 3.1) that contribute to the energy available for melt (Q_{tot}) are solar shortwave radiation (Q_s), longwave thermal radiation (Q_l), turbulent heat fluxes (i.e. sensible heat Q_H & latent heat Q_L), heat from precipitation (Q_p) and geothermal heat (Q_G).

$$Q_{tot} = Q_s + Q_l - Q_H - Q_L + Q_p - Q_G \quad 3.1.$$

$$\begin{cases} Q_{tot} > 0, ground\ warming \\ Q_{tot} < 0, ground\ cooling \end{cases}$$

The debris surface heat flux is then

$$Q_{G_{surf}} = Q_s + Q_l - Q_H - Q_L + Q_p \quad 3.2.$$

In most cases, heat from precipitation and geothermal sources are quite small in comparison to the other sources. Collecting data on all of the energy budget components can be quite costly as most weather stations can cost 1000s of dollars. There are many other equations which can be used to model certain energy fluxes based on other collected data (e.g., turbulent fluxes and long wave radiation) however some of these require the knowledge of many physical parameters which may be difficult to determine. Early studies on the surface energy budget were done with weather stations and the collected data were then applied to different melt models (Hay and Fitzharris 1988, Braithwaite and Olesen 1990, Oerlemans 1992, Oerlemans and Klok 2002, Hock 2005). The downside to this is that the data are point specific and hard to extrapolate across a large glacier surface. More recent approaches have attempted to extract surface energy data from satellite imagery (Gratton et al. 1993, Roerink et al. 2000) however this only uses an instantaneous value and cannot show changes on a small

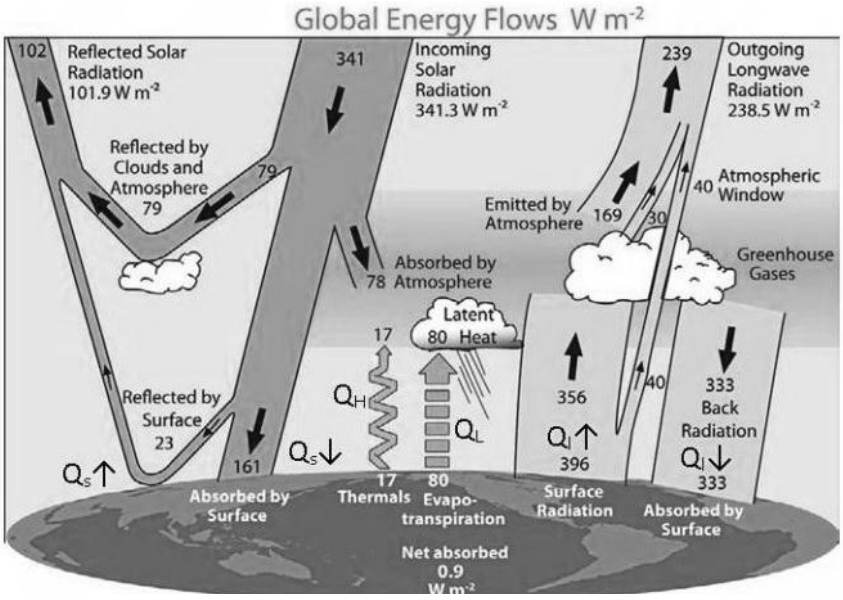

Figure 2: Annual global energy fluxes adapted from Trenberth et al. 2009.

time scale. A new annual average global energy flux was computed using measurements and models in combination with remote sensing data. The annual average magnitudes of the different energy budget components can be seen in **Error! Not a valid bookmark self-reference.**.

3.1.1 Radiative Heat Flux

Shortwave Radiation

Solar radiation that makes it through the atmosphere has been shown to be the dominant energy source causing melt on glaciers (Braithwaite and Olesen 1990, Pellicciotti et al. 2005). The net solar radiation that does make it to any point on earth is made up of three components, direct radiation, diffuse radiation and reflected radiation. The radiation coming from the direct beam of the sun's light is referred to as direct radiation. Radiation from the sky and from clouds (when they are present) is referred to as diffuse radiation. This can be thought of as the light in the sky when the sun is not directly visible.

Calculating the amount of direct radiation on a plane is relatively simple and involves performing some calculations on the sun's position relative to the location of the plane on Earth. However it is more difficult to calculate individual components of the total radiation and many models or empirical equations have been developed (Bindi et al. 1992, Brock et al. 2000a, Hock 2005, Pellicciotti et al. 2005, Zakšek et al. 2005, Keller and Costa 2009). Finally there is reflected solar radiation or radiation that travels to a point by being reflected off of other surfaces (e.g. terrain, vegetation, buildings). The amount of reflected radiation also depends on the reflection surface, specifically the angle and the albedo.

The total amount of absorbed solar radiation depends on the surface albedo, or the ratio of the reflected radiation to the total incoming radiation as seen in Equation 3.3.

$$\propto = \frac{Q_s\uparrow}{Q_s\downarrow} \quad 3.3.$$

Where $Q_s\uparrow$ is the reflected radiation and $Q_s\downarrow$ is the total incoming radiation. Net shortwave radiation (Q_s) can be calculated using

$$Q_s = Q_s \downarrow (1 - \alpha) \quad 3.4.$$

Simply put, the higher the albedo the lower the Q_s and vice versa. Some common albedo values for various glacial surfaces can be seen in Table 1 below. It is not just the reflectance of the debris surface that has effects on the albedo but also, as can be seen below, the presence of water or even debris intermixed with the snow or ice can reduce the albedo drastically thereby increasing absorbed SW radiation.

Table 1: Surface albedo values of different snow and ice types (Cuffey and Paterson 2010).

Surface type	Minimum	Maximum
Fresh dry snow	0.75	0.98
Old clean dry snow	0.70	0.85
Old clean wet snow	0.46	0.70
Old debris-rich dry snow	0.30	0.60
Old debris-rich wet snow	0.30	0.50
Clean firn	0.50	0.65
Debris-rich firn	0.15	0.40
Superimposed ice	0.63	0.66
Blue ice	0.60	0.65
Clean ice	0.30	0.46
Debris-rich ice	0.06	0.30

Longwave Radiation

All surfaces emit energy in the form of longwave radiation. The irradiance or heat emitted per unit area is described in the Stefan-Boltzmann equation as being directly proportional to the forth power of the object's absolute temperature

$$I^* = \varepsilon\sigma T_{surf}^4 \qquad 3.5.$$

$$\begin{cases} \varepsilon = 1, & blackbody \\ 0 < \varepsilon < 1, & greybody \end{cases}$$

Where I^* is the irradiance (energy given off), ε is the emissivity and σ is the Stefan-Boltzmann constant$\left(5.67 \times 10^{-8}\,\frac{W}{m^2K^4}\right)$. An object that emits all of its available radiation perfectly is known as a blackbody, whereas an object that emits only part of its available radiation is known as a greybody. Earth's surface and atmosphere both emit thermal energy in the form of longwave radiation, Q_l.

The magnitude of longwave radiation emitted from the atmosphere is a function primarily of the air temperature, CO_2 and O_3, and concentration of water vapor (e.g. clouds). Without direct measurements it is one of the more difficult energy sources to model. A simple formula for the calculation of $L\downarrow$ is,

$$L\downarrow = \varepsilon_c\sigma T_{air}^4 F(n) \qquad 3.6.$$

$$\varepsilon_c = (1 + 0.275 * c)\left(1 - 0.261e^{\left(-7.77*10^{-4}(273.15-T_{air})\right)}\right)$$

where ε_c is the clear sky emissivity and F (n) and c are cloud factors. Numerous equations have also been developed to calculate ε_c (Konig-Langla and Augstein 1994, Hock 2005) but for the purpose of this study and keeping with a simplistic approach, cloud cover parameters have been neglected in favor of Equation 3.5 using T_{air} in place of T_{surf}. For ε_c an equation from Parkinson and Washington (1979) has been used, assuming zero cloud cover.

3.1.2 Turbulent Heat Flux

The exchanges of heat between the atmosphere due to temperature differences and moisture concentrations are referred to as sensible heat flux and latent heat flux respectively.

Calculating these fluxes with minimal error involves gathering data on numerous different atmospheric and surface parameters (e.g. surface roughness length (z_0), eddy viscosities and vertical wind profiles) which can be expensive. Other approaches have simplified these formulae and use what is known as the bulk aerodynamic method which only needs T_s, $T_a(z)$, $T_h(z)$, $U(z)$ and z_0 (Brock et al. 2006). From Oerlemans (2010) and Cuffey and Paterson (2010) we find equations for both sensible and latent heat flux as

$$Q_H = \rho c_p C_s u(T_a(z) - T_s) \quad 3.7.$$

and

$$Q_L = \rho L_e C_l u(q_a(z) - q_s) \quad 3.8.$$

Where ρ is the density of air $\left(1.2\ \frac{kg}{m^3}\right)$, c_p is the specific heat capacity of air $\left(1003\ \frac{J}{kgK}\right)$, C_s and C_l are the transfer coefficients, L_v is the latent heat of evaporation of water $\left(2.49\ x\ 10^6\ \frac{J}{kg}\right)$, u is the wind speed $\left(\frac{m}{s}\right)$, q_a is the specific humidity at height (z) and q_s is the surface specific humidity $\left(\frac{g}{m^3}\right)$. Cuffey and Paterson go one step further in that they rewrite Equations 3.7 and 3.8 in the "Flux Gradient Form" where saturation vapor pressure (SVP) is used in place of humidity since SVP is a function of T_a.

$$Q_H = \rho\left(\frac{P}{P_0}\right) c_p C^* u(T_a(z) - T_s) \quad 3.9.$$

$$Q_L = \left(\frac{0.622\rho}{P_0}\right) L_e C^* u(e_a(z) - e_s) \quad 3.10.$$

The fluxes are now calculated using P_0, the standard air pressure at sea level $(1.013\ x\ 10^5\ Pa)$, air pressure at the site (P), saturation vapor pressure at both height (z) and the surface $(e_a(z), e_s)$ and a dimensionless transfer coefficient (C^*) which is determined from the following equation

$$C^* = \frac{k_0^2}{\left[ln\left(\frac{z}{z_0}\right)\right]^2} \quad 3.11.$$

where k_0 is the von Kármán's constant and z is the height of measurements. While the von Kármán's constant is often given a value of 0.4 for this study a value of 0.39 has been used as the constant has been determined to be closer to .39 than .4 (Andreas 2009). Brock et al. (2000b) determined that while Equations 3.7 and 3.8 are reasonable to use, the accuracy depends on correct measurements of z_0. They noted that if z_0 is changed by an order of magnitude (in most cases this would be a change in mm) it could cause a difference of almost 100% in turbulent flux calculations. Cuffey and Patterson (2010) state that the heat exchange between the surface and air is controlled by three factors:

1. Wind speed at height z above the surface.
2. Surface roughness length (thought of as the height of undulations on a surface).
3. The stability of the atmosphere (i.e. whether or not there is buoyant vertical mixing).

and of these three factors, number 1 is "the most important". Surface roughness values for varying ice and snow surfaces can be found in Brock et al. (2000b) and are summarized by surface type in Brock et al. (2006). These values can vary anywhere from 0.0002m for fresh snow to 0.03m for snow penitentes. Glacial ice values rage from 0.0001m to 0.08m, the latter being "very rough glacier ice". For calculating z_0 one can use the approach of Takeuchi et al. (2000) where they calculated z_0 by looking at the vertical wind profile between two heights where,

$$z_0 = e^{\left[\frac{(U_2 lnz_1 - U_1 lnz_2)}{(U_2 - U_1)}\right]} \quad 3.12.$$

And U_2, U_1, z_2, and z_1 are the wind speeds (U) at two heights (z). For this study z_0 has been set at 0.01m, following Nicholson and Benn (2006) who calculated quite reasonable results when modeling ablation under debris cover on the Larsbreen glacier just one valley away from this study site.

3.1.3 Precipitation and Geothermal Heat Flux

Precipitation Heat

Precipitation contributes to the flux of heat through a debris layer by water infiltration down between grain boundaries where it releases heat to the surrounding debris. In Reid and Brock (2010) the heat delivered from precipitation to the surface is given by

$$Q_p = \rho_w c_w w(T_r - T_s) \qquad 3.13.$$

Where ρ_w is the density of water$\left(1000\ \frac{kg}{m^3}\right)$, c_w is the specific heat capacity of water $\left(4181\ \frac{J}{kgK}\right)$, w is the precipitation rate in$\left(\frac{m}{s}\right)$ and T_r is the temperature of the rain. For their study they assume a rain temperature equal to the air temperature due to difficulty in obtaining this measurement in the field.

If the debris temperature is colder that the precipitation temperature then as the moisture percolates through the layer it releases its heat and warms the layer. However if the debris layer is quite cold and contains interstitial ice the precipitation may only warm a certain small area above this ice and not percolate further. Depending on how cold the debris is, this may cause the precipitation to warm the ice yet not melt it, which can lead to more formation of possible ice lenses or interstitial ice within the debris layer.

If the debris temperature is warmer than the precipitation then it will give off heat to warm the moisture as it infiltrates. In this case there is a good chance the moisture will make it to the ice-debris interface and contribute to ice melt. However, in general, the heat delivered by precipitation is often quite negligible and for this study it has been disregarded.

In some regions it is also quite difficult to monitor the precipitation. For example on Svalbard where much of the annual precipitation falls as snow and the weather is quite erratic, getting accurate measurements of precipitation is hindered by the redistribution due to wind.

Geothermal Heat

Geothermal heat is the heat produced by the Earth that is conducted upwards from the core to the surface. For this study, since the basal conditions are not incorporated into this model and the focus is on the surface of the ice, the flux of geothermal heat has been set at a constant value of 0.06 $\frac{W}{m^2}$. This is the global average geothermal heat flux as determined by data from boreholes throughout the world (Rial 2011).

3.2 Effects of Debris Cover on Ablation

With the introduction of debris to the surface of a glacier come changes in how the atmospheric heat is exchanged. Glacier ice can be ablated by means of melting through heat conduction, sublimating (change from ice to vapor), wind scouring and calving. When debris is present the effects of many of these processes are dampened. While calving can still occur on debris covered glaciers, in the form of ice cliff calving into supraglacial lakes or moraine dammed lakes, the contribution to melt from wind scouring and sublimation are reduced substantially. Precipitation and warm air masses can still affect the ice surface by being transmitted through the open spaces between debris. Aside from these, the most significant process that contributes to melt is conduction (Nicholson 2004). Therefore the two main effects of a debris layer on changes in ablation are by influencing the rate at which heat is transferred to the ice surface through the previously mentioned processes, and by causing a change in the surface albedo, thereby reflecting more of the incoming shortwave radiation.

3.2.1 Albedo Changes

Many studies have been done to look at the changes in the surface albedo of glaciers with the addition of debris. Of these studies one of the most important was that of Østrem (1959) and his measurements of ablation below debris layers of varying thickness. Through this study he was able to show that as the thickness increases the daily melt rate decreases in a decaying exponential fashion.

Since his pioneering work in 1959 many scientists have adapted his methods to other glaciers and have come up with melt rate curves as a characteristic of individual glaciers. These curves

vary both in magnitude of melt rate and influence of debris thickness. One of the most notable characteristics of the Østrem curve is the zone between 0 and ~2cm debris thickness where the melt rate actually goes up and then back down at ~2cm to equal the same melt as that of debris free ice. This thickness is widely known as the "critical thickness".

As debris is added to the surface the albedo begins to change and becomes almost an average, over a certain area, of debris and ice. With very thin cover, such as that of fine dust, heating of the lower albedo material causes the formation of cryoconites, or little pockets, which collect the material into clumps which melt further into the ice. On the other hand, if the debris is not fine, yet is still sparsely distributed on the surface, one can expect to see rock tables form where the ice around a rock melts but the ice below does not melt as fast thereby leaving the rock elevated above the lowered ice surface. In some cases this can be quite extreme.

After the debris has passed the "critical thickness" it begins to insulate the ice rather than increase melt. This is due to the albedo becoming totally that of the debris, creating a continuous layer of lower thermal conductivity material above the ice.

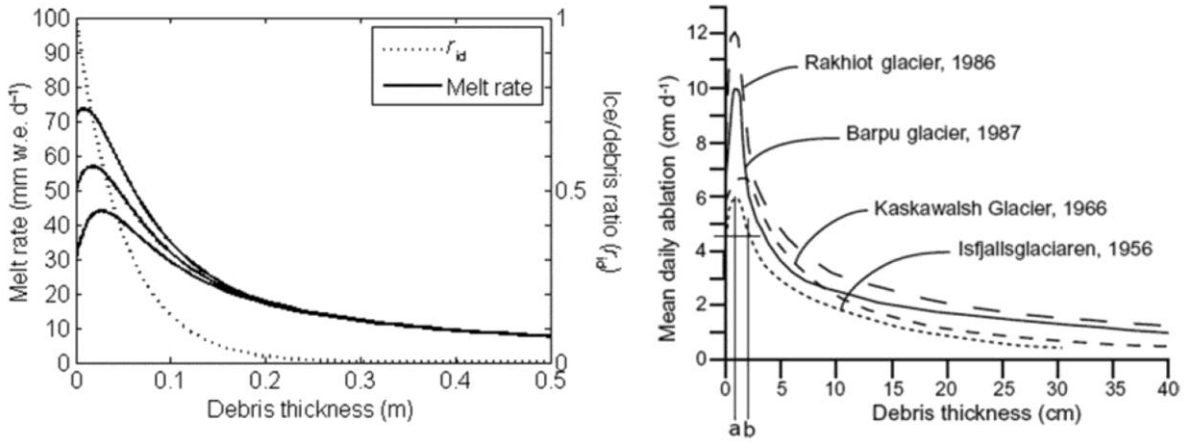

Figure 3: Modeled melt rate from Miage glacier showing Østrem curve from Reid and Brock (2010)(left) and actual melt rates from various glaciers (Nicholson and Benn 2006).

This phenomena has been developed into models such as Reid and Brock's (2010) debris energy-balance model (DEB). DEB is a physically based model where based on atmospheric data collected on the Miage glacier over three years, the surface temperature is calculated using iterative methods and the resulting surface temperature is then fed into a one-dimensional heat model which is then solved using the Crank-Nicolson method of finite

difference approximation to solve the one-dimensional heat equation. They were able to reproduce the signature rising limb of the Østrem curve by setting melt equal to a combination of debris free melt and debris covered melt such that

$$M = r_{ice}M_{bare} + (1 - r_{ice})M_{debris} \quad 3.14.$$

where

$$r_{ice} = e^{-Cd} \quad 3.15.$$

and C is a constant and d is the debris thickness. So as debris thickness increases, r_{ice} decreases exponentially to zero where all that remains is M_{debris}. They were able to produce reasonable results as can be seen in Figure 3. The curves produced using Equation 3.14 fit quite well to the observed data on the right hand plot in Figure 3. The value of "C" is the determining factor in how steep the curve is, or in other words how quickly the melt becomes M_{debris}. In the right hand plot above it can be seen that glaciers in different regional settings have different curves. Some may exhibit a larger critical thickness while others may have the same critical thickness yet a higher maximum melt.

For the purpose of this study no implementation has been made to adjust the surface albedo in response to thickening debris layers. For very thin debris the albedo is still that of total debris coverage.

4 Developing the Heat Flux Model

4.1 Previous Work With Melt Modeling

The early studies of the interaction between glaciers and surface energy budget began in the first half of the 20th century. Numerous researchers began publishing their findings, such as Finsterwalder and Schunk (1887) and the connection between air temperature and ablation, Hess (1904) and the importance of radiation in glacial ablation, and Angstrom (1933) and the importance of air temperature, wind and radiation on melting (Hock 2005). One major contribution to the early study of atmosphere/glacier interactions came from the Norwegian-Swedish Spitsbergen Expedition of 1934. For two months research was carried out measuring radiation and turbulent heat exchanges at the glacier surface (Olsson and Ahlmann 1936).

During the latter part of the 20th century many studies were carried out on glaciers in Switzerland, Austrian and the Scandinavian countries, expanding the scientific community's understanding of energy fluxes, glacier mass balance, melt water production and how topographic variables affect mass balance. It wasn't until the 1960's that computer models started to be created and used as simple accumulation and ablation models to models bringing together the whole energy balance regime (Hock 2005).

One commonly used melt model is that developed by Nakawo and Young (1981), where under the assumption of a daily average linear temperature profile, which means a constant thermal gradient, the daily average energy that reaches the ice surface is equal to,

$$Q_m = k\left(\frac{T_s - T_i}{z}\right) \qquad 4.1.$$

where the numerator is the difference between the surface temperature and the ice temperature and z is the debris thickness. Using this equation, on must assume the ice surface is at 0°C and the debris thermal conductivity is constant.

In the last few years two distinct types of models have become commonly used. These are the energy balance models and temperature index models. Both models have been shown to

produce good results yet the temperature index model is a very simplified model which combines surface energy exchanges together whereas the energy balance model is a much more physical representation of the processes occurring at the surface.

4.2 Model Development

For this study a computer model has been developed following the approach of Recktenwald (2011b) and the demoCN.m model (Recktenwald 2011a). In the original demoCN.m model the heat equation was solved for a state of zero flux boundary conditions (Dirichlet) and an initial vertical temperature specified by the user. For this study a more complex model has been built onto the essential demoCN.m model where flux boundary conditions (Neumann) have been included at both the surface and the bottom.

The heat equation is solved for a specified time period through a one-dimensional debris layer using finite difference approximations. Fourier's law states the heat flowing across a surface, Q, is equal to the negative temperature gradient, $\frac{\partial T}{\partial z}$ times the thermal conductivity, k.

$$Q = -k\frac{\partial T}{\partial z} \qquad 4.2.$$

Equation 4.2 is the basis for the linear thermal gradient method of modeling melt by setting ∂z equal to the debris thickness and ∂T as the difference between the surface temperature and the ice temperature (assumed to be 0°C). Expanding this equation through the use of calculus and allowing ∂z and ∂T to become small finite values across both depth and time, and through some algebraic manipulation, the three dimensional form, which is commonly referred to as the convection-diffusion equation, is shown.

$$\frac{\partial T}{\partial t} = \alpha\nabla^2 T + T \cdot \vec{v}\nabla \qquad 4.3.$$

where the LHS term is the change in temperature with time and the first term on the RHS is the diffusivity (α) multiplied by the divergence (or three dimensional second derivative over space) of the temperature gradient. This term is also known as the conduction (sometimes diffusion) term. Transport of heat by means of conduction involves heat being transferred

from one object to another solely by contact and involves no macro scale physical movement of the object. The second term on the RHS is the term for advection. For this study advection, or the transport of heat through means of fluid (gas or liquid) flow, has been disregarded. However this is not realistic as heat can be transported by advection through a debris layer by air flow or heat stored in precipitation percolating through the layer as mentioned previously. By dropping the advection term in Equation 4.3 we find the following.

$$\frac{\partial T}{\partial t} = \alpha\left(\frac{\partial^2 T}{\partial x^2} + \frac{\partial^2 T}{\partial y^2} + \frac{\partial^2 T}{\partial z^2}\right) \qquad 4.4.$$

Equation 4.3 gives the 3-dimensional equation for heat flow. For this study the terms representing heat flow along the transvers or longitudinal plane as seen in Figure 4 are dropped and disregarded. It is assumed that in the one-dimensional model heat flux is only done in the direction normal to the debris surface (Z).

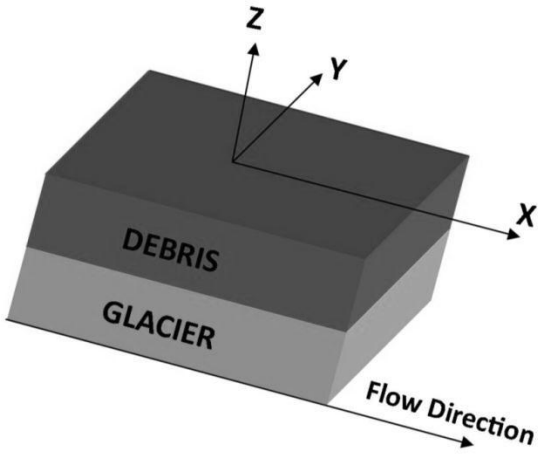

Figure 4: Geometry of debris covered glacier system. X being along the longitudinal direction, Y being along the transverse direction and Z being along the vertical direction.

The equation then simplifies down to the basic one dimensional partial differential heat equation which is the basis for the model, where the change in temperature with time (LHS) $\left(\frac{K}{s}\right)$ is equal to the vertical heat flux (RHS) $\left(\frac{K}{m^2}\right)$ times α $\left(\frac{m^2}{s}\right)$.

$$\frac{\partial T}{\partial t} = \alpha\left(\frac{\partial^2 T}{\partial z^2}\right) \quad 4.5.$$

The diffusivity is dependent on the intrinsic physical properties of the debris such that

$$\alpha = \frac{k}{c_p \rho} \quad 4.6.$$

where k has units of $\left(\frac{W}{mK}\right)$, c_p $\left(\frac{J}{kg\ K}\right)$ is the specific heat capacity and ρ $\left(\frac{kg}{m^3}\right)$ is the density of the material. The bottom two terms of Equation 4.6 are often combined to one single term known as the volumetric heat capacity (C_v) $\left(\frac{J}{m^3 K}\right)$. The diffusivity shows at what rate a material can adjust its temperature to the surrounding temperatures. Debris layers do not have constant physical properties, in fact in many cases the debris is a combination of material from the surrounding areas and with the inclusion of water (i.e. debris moisture content), ice (e.g. interstitial, ice lenses) and even air within grain boundaries, these properties for the debris layer as a whole become difficult to generalize. However for this model the default values for k, c_p and ρ are 1.6 $\left(\frac{W}{mK}\right)$, 900 $\left(\frac{J}{kgK}\right)$ and 2700 $\left(\frac{kg}{m^3}\right)$, respectively as used by Nicolson and Benn (2006).

4.2.1 Finite Difference Method

Solving the heat equation is not impossible given the right boundary conditions. For the model presented here, Neumann boundary conditions have been applied allowing for both surface flux and basal flux. In order to solve the PDE, a method using finite differences has been adapted. This method involves turning the space being modeled over into a series of finite points, in this case across time and space, creating the "mesh". The finite equations use a combination of values at mesh points to calculate the value at another point. In Figure 5 below, 3 common meshes are shown, each with arrows indicating which nodes are used for each method.

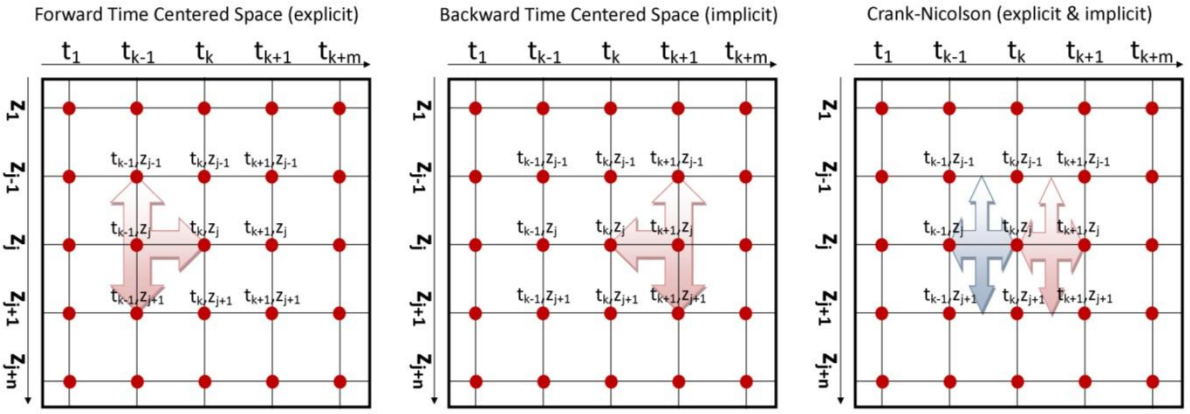

Figure 5: Finite mesh layout for different schemes showing which nodes are involved in each. The explicit method involves using values at t_k to find values at the next timestep t_{k+1} and vice versa for the implicit method.

The model runs over j depth nodes and k time nodes. The index notation adapted is as such

$$T_{j+1}^{k+1} \rightarrow Temperature\ at\ depth\ z_{j+1}\ at\ time\ t_{k+1} \qquad 4.7.$$

The differentials in Equation 4.5 are then simplified through the use of Taylor expansions, whereby the change from z to Δz is approximated in a series of increasing order. The accuracy of the expansions increase as$\Delta z \rightarrow 0$, or the number of higher order terms approaches ∞. By combining different expansions, different schemes for approximating the heat flux at each node can be developed. Three common schemes (Figure 5) are Forward Time Center Space (FTCS), Backwards Time Center Space (BTCS) and the Crank-Nicolson (CN) method (Crank and Nicolson 1947) which uses the average of the spatial differences at t_k and t_{k+1}. The two Taylor expansions used to derive each of the mentioned schemes are a forward time expansion and a backward time expansion such as

$$T(z+\Delta z) = T(z) + \frac{\Delta z}{1!}\frac{\partial T}{\partial z}\Big|_{z_j} + \frac{(\Delta z)^2}{2!}\frac{\partial^2 T}{\partial z^2}\Big|_{z_j} + \frac{(\Delta z)^3}{3!}\frac{\partial^3 T}{\partial z^3}\Big|_{z_j} + \frac{(\Delta z)^4}{4!}\frac{\partial^4 T}{\partial z^4}\Big|_{z_j} \ldots + \frac{(\Delta z)^n}{n!}\frac{\partial^n T}{\partial z^n}\Big|_{z_j} \qquad 4.8.$$

and.

$$T(z-\Delta z) = T(z) - \frac{\Delta z}{1!}\frac{\partial T}{\partial z}\Big|_{z_j} + \frac{(\Delta z)^2}{2!}\frac{\partial^2 T}{\partial z^2}\Big|_{z_j} - \frac{(\Delta z)^3}{3!}\frac{\partial^3 T}{\partial z^3}\Big|_{z_j} + \frac{(\Delta z)^4}{4!}\frac{\partial^4 T}{\partial z^4}\Big|_{z_j} \ldots - \frac{(\Delta z)^n}{n!}\frac{\partial^n T}{\partial z^n}\Big|_{z_j} \qquad 4.9.$$

Solving both of the above equations for $\frac{\partial T}{\partial z}\Big|_{z_j}$, the change in temperature with depth at some node z_j is,

$$\left.\frac{\partial T}{\partial z}\right|_{z_j} = \frac{T(z+\Delta z) - T(z)}{\Delta z} + \mathcal{O}(\Delta z) \tag{4.10.}$$

and

$$\left.\frac{\partial T}{\partial z}\right|_{z_j} = \frac{T(z) - T(z-\Delta z)}{\Delta z} + \mathcal{O}(\Delta z) \tag{4.11.}$$

which are both 1st order differences. The higher order terms are combined using Cauchy's mean value theorem to represent the resulting error due to approximating the differentials (i.e. truncation error). The truncation error for the above two equations is proportional to Δz and is reduced as Δz approaches zero. By combining Equations 4.8 and 4.9 it is also possible to derive centered and higher ordered differences.

$$T(z+\Delta z) + T(z-\Delta z) = 2T(z) + \frac{2(\Delta z)^2}{2!}\left.\frac{\partial^2 T}{\partial z^2}\right|_{z_j} + \frac{2(\Delta z)^4}{4!}\left.\frac{\partial^4 T}{\partial z^4}\right|_{z_j} \ldots - \frac{2(\Delta z)^n}{n!}\left.\frac{\partial^n T}{\partial z^n}\right|_{z_j}\Bigg|_{n=even} \tag{4.12.}$$

$$T(z+\Delta z) - T(z-\Delta z) = \frac{2\Delta z}{1!}\left.\frac{\partial T}{\partial z}\right|_{z_j} + \frac{2(\Delta z)^3}{3!}\left.\frac{\partial^3 T}{\partial z^3}\right|_{z_j} \ldots + \frac{2(\Delta z)^n}{n!}\left.\frac{\partial^n T}{\partial z^n}\right|_{z_j}\Bigg|_{n=odd} \tag{4.13.}$$

Solving Equation 4.12 for $\left.\frac{\partial^2 T}{\partial z^2}\right|_{z_j}$ and Equation 4.13 for $\left.\frac{\partial T}{\partial z}\right|_{z_j}$ the following 2nd and 1st order central difference equations are found.

$$\left.\frac{\partial^2 T}{\partial z^2}\right|_{z_j} = \frac{T(z+\Delta z) - 2T(\Delta z) + T(z-\Delta z)}{\Delta z} + \mathcal{O}(\Delta z)^2 \tag{4.14.}$$

$$\left.\frac{\partial T}{\partial z}\right|_{z_j} = \frac{T(z+\Delta z) - T(z-\Delta z)}{2\Delta z} + \mathcal{O}(\Delta z)^2 \tag{4.15.}$$

Translating Equations 4.10, 4.11, 4.14 and 4.15 into finite notation using a mesh notation of j depth nodes and k time nodes, the forms of the forward, backward and Crank-Nicolson schemes are found.

$$\frac{T_j^{k+1} - T_j^k}{\Delta t} = \alpha \frac{T_{j+1}^k - 2T_j^k + T_{j-1}^k}{\Delta z} + \mathcal{O}(\Delta t) + \mathcal{O}(\Delta z)^2 \quad Forward\ Time, Center\ Space \tag{4.16.}$$

$$\frac{T_j^k - T_j^{k-1}}{\Delta t} = \alpha \frac{T_{j+1}^k - 2T_j^k + T_{j-1}^k}{\Delta z} + \mathcal{O}(\Delta t) + \mathcal{O}(\Delta z)^2 \quad Backwards\ Time, Center\ Space \tag{4.17.}$$

$$\frac{T_j^{k+1} - T_j^k}{\Delta t} = \alpha \frac{T_{j+1}^{k+1} - 2T_j^{k+1} + T_{j-1}^{k+1}}{2\Delta z} + \alpha \frac{T_{j+1}^k - 2T_j^k + T_{j-1}^k}{2\Delta z} + \mathcal{O}(\Delta t)^2 + \mathcal{O}(\Delta z)^2 \quad CN \tag{4.18.}$$

While under certain conditions all three methods can yield highly accurate results, only the backwards time center space and Crank-Nicolson methods are unconditionally stable. However as both methods have spatial truncation errors proportional to Δz^2 the Crank-Nicolson method has a temporal error proportional to Δt^2. This second order term makes the total truncation error for the Crank-Nicolson method orders of magnitude smaller than the other two (Recktenwald 2011c) and has therefore been used in this study.

4.2.2 Solving the Finite Difference Model

To solve Equation 4.18 it first needs to be rearranged to have all the terms of timestep t_{k+1} on the LHS and t_k on the RHS. Dropping the truncation error terms it becomes

$$a_j T_{j-1}^{k+1} + b_j T_j^{k+1} + c_j T_{j-1}^{k+1} = -a_j T_{j+1}^k + \left(\frac{1}{\Delta t} - \frac{\alpha}{\Delta z^2}\right) T_j^k - c_j T_{j-1}^k \tag{4.19.}$$

$$a_j = c_j = \frac{-\alpha}{2\Delta z^2}$$

$$b_j = \frac{1}{\Delta t} + \frac{\alpha}{\Delta z^2}$$

$$d_j = -a_j T_{j+1}^k + \left(\frac{1}{\Delta t} - \frac{\alpha}{\Delta z^2}\right) T_j^k - c_j T_{j-1}^k$$

This is the form when solving for zero flux conditions. For the purpose of this study an additional constant term has been added which allows for the flux across the boundaries, however due to copyright reasons the steps cannot be shown here (Recktenwald 2011c). Combining the equations in Equation 4.19 a group of linear equations is found for each step. These can be solved using linear algebra after forming the matrices. It should be noted however b_1, c_1, and b_n have different values from $a_{2:n-1}$,$b_{2:n-1}$,$c_{2:n-1}$ due to the flux boundary conditions. At the first and last depth node the constant is a function of the time varying heat flux from the atmosphere and the ground.

$$\begin{bmatrix} b_1 & c_1 & 0 & & & 0 & 0 & 0 \\ a_2 & b_2 & c_2 & \cdots & & 0 & 0 & 0 \\ 0 & a_3 & b_3 & & & 0 & 0 & 0 \\ & \vdots & & \ddots & & \vdots & & \\ 0 & 0 & 0 & & b_{n-2} & c_{n-2} & 0 & \\ 0 & 0 & 0 & \cdots & a_{n-1} & b_{n-1} & c_{n-1} & \\ 0 & 0 & 0 & & 0 & a_n & b_n & \end{bmatrix} \begin{bmatrix} T_1 \\ T_2 \\ T_3 \\ \vdots \\ T_{n-2} \\ T_{n-1} \\ T_n \end{bmatrix} = \begin{bmatrix} d_1 \\ d_2 \\ d_3 \\ \vdots \\ d_{n-2} \\ d_{n-1} \\ d_n \end{bmatrix} for\ n = \#Z\ nodes \quad 4.20.$$

The tridiagonal matrix is factored into an upper and lower matrix using what is known as LU decomposition. During the model run this is done for each timestep using tridiagLU.m (Recktenwald 2011d). After the decomposition the values are then used in tridiagLUsolve.m (Recktenwald 2011e) to find T^n from T^{n+1}.

4.2.3 Calculating Melt

The output temperature data from the model is in the form of an n x m matrix where n is the number of depth nodes and m is the number of time nodes. By using the gradient function in MATLAB the temperature gradients with respect to time and depth are found. Using Equation 4.2 it is possible to determine the heat flux at the ice depth for a period of time and thus determine the melt rate M

$$-k\,\frac{\partial T}{\partial z} = Q_{melt} \implies M = \left(-k\,\frac{\partial T}{\partial z}\right)\left(\frac{1}{\rho_{ice} L f_{ice}}\right)\left[\frac{m}{s}\right] \quad 4.21.$$

where ρ_{ice} is the density of ice ($916.7\left(\frac{kg}{m^3}\right)$) and Lf_{ice} is the latent heat of fusion of water ($334000\left(\frac{J}{kg}\right)$). Simply multiplying the melt rate by Δt will yield the amount of melt per timestep.

$$M = \frac{Q_{melt}\Delta t}{\rho_{ice} L f_{ice}} \quad 4.22.$$

Storing these values and adding them up gives the cumulative melt for the given period. In the case of negative melt, or the removal of enough heat from some point z to induce refreezing, the melt is considered zero and refreezing and the release of latent heat is ignored. It is important to point out that while this method does simplify the model, the presence of water within the debris layer can cause ice to form within grain boundaries, or even as ice lenses, let

alone refreezing to the glacier surface. This can cause heaving of the debris layer and changes in the geometry of the system. To accurately model these phenomena, data on the debris moisture content would be needed.

4.3 MODEL.m

4.3.1 Initial MODEL.m

The basic code for the model *MODEL.m* requires the user to input all the parameters of the run into one command line as seen in Diagram 1. *MODEL.m* runs the model using synthetic data such as sinusoidal energy inputs. The input parameter "ENERGY" allows the user to choose which energy source to use. Using values of 1-5, the choices are seen below in Table 2.

Table 2: ENERGY surface energy input choices.

1	2	3	4	5
Shortwave	Longwave	Short & Longwave	Shortwave, Longwave & Sensible Heat	Specific Surface Temperatures

The input parameters Days, sec, Nz and Z specify the model geometry (i.e. number and size of depth and time nodes). One key thing to keep in mind when performing model runs is that the truncation errors that propagate through during each iteration go to zero in proportion to the size of $\Delta z^2$and Δt^2 as explained in Section 4.2.1. For this reason the total depth (Z) should be varied from a thin debris layer up to 2m max. This allows the mesh to stay the same size and therefore Δz^2 stays << 1. Keeping the timestep small (i.e. 6-120 (sec)) also helps to reduce the error significantly.

The basic model run assumes a debris layer of constant physical parameters (i.e. k, c_s, and ρ) which are specified by the user. However, in order to test the effect of multiple layers containing different parameters, a script was built into *MODEL.m* to accept specifications of special layer geometry (i.e. multiple layers, beginning, end, and physical properties).

The energy inputs are built off Equations 3.4, 3.6, 3.9 and 3.10, and use the wave form specified by the user. For more realistic synthetic data the sinusoidal waveform is used, yet when comparing this study's initial results to Reznichenko et al. (2010), a square wave which mimics their laboratory experiment of a 12hr heating phase and a 12hr cooling phase, has been implemented. The input parameter "Duty Cycle" is used in combination with the square waveforms. The duty cycle of a square wave is the amount of time during each period in which the wave is on or off so to speak. This implementation allows the user to study changes in hypothetical hours of energy input (analogous to hours of sunlight).

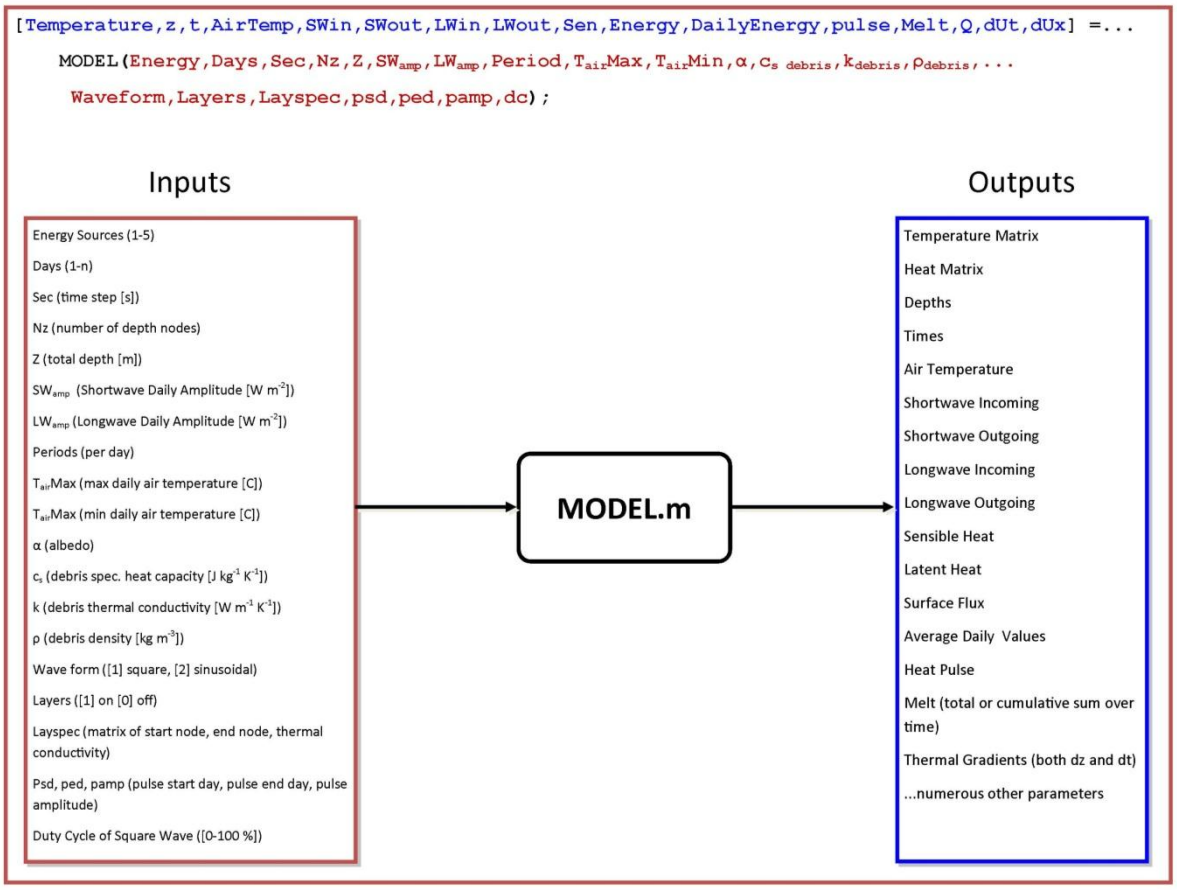

Diagram 1: The upper line of text illustrates the command line input for *MODEL.m* while the flow diagram below explains what each input parameter is and what the subsequent output data is.

The outputs listed in Diagram 1 can be varied quite easily for numerous reasons. The diagram just illustrates the variety of outputs that can be achieved. Having numerous outputs sent to the workspace fills the computer's memory quite quickly, especially since the model can easily

generate matrices of data up to 200 x 144000 for a run of 100 days and Δt = 60sec and 200 depth nodes for Z=1m yielding a Δz = 5mm.

The model can also be run using simple 5 line scripts with for loops to alter variables and perform multiple runs while changing values. The last lines of *MODEL.m* are set up to write which ever output is needed to a user specified text file (*.txt) for further analysis.

4.3.2 MODEL.m Testing

Cumulative Melt vs. Δt

Initial model tests involved measuring the accuracy of model output while varying input parameters. In order to make sure the model is working properly comparative tests were performed on simulations for 10 day melt. All initial tests followed the command line input of

MODEL(4,10,time(i),500,j,500,300,1,15,-5,.18,900,2.4,2700,2,0,0,0,0,0)

where i and j change the timestep and Z respectively. The first test was an analysis of the changes in 10 day cumulative melt with different Δt values.

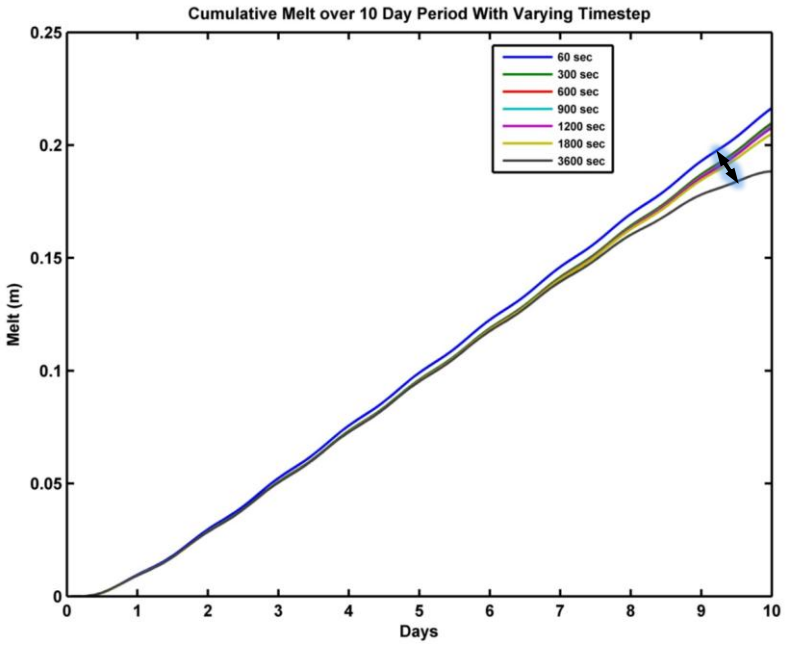

Figure 6 : Cumulative melt over a 10 day synthetic period. The colored lines represent the different time steps used for each run.

The truncation error can clearly be seen growing in Figure 6 as Δt increases from 60 sec to 3600 sec. As $\Delta t \rightarrow 0$ the error is supposed to grow smaller and this is clearly what is seen in the case of the smaller time steps as they converge on each other. The dark arrow at the end of the lines shows the gap between the 60sec run and the 3600sec run. Notice how the 3600sec run was beginning to diverge from the general trend of all lines with an increasing rate during the 8th-10th days.

Daily Melt Rate vs. Δt

The next test was to analyze how the model performed under varying debris thicknesses. For this test the model was run using the same parameters as were used for Figure 6 yet Z was varied from .01m to 1m, resulting in a Δz of .00001m to .001m. The resulting plot shows the melt rate for the 10th day, assuming the model has run up to a steady state by the 10th day yielding synthetic Østrem curves for the debris layer.

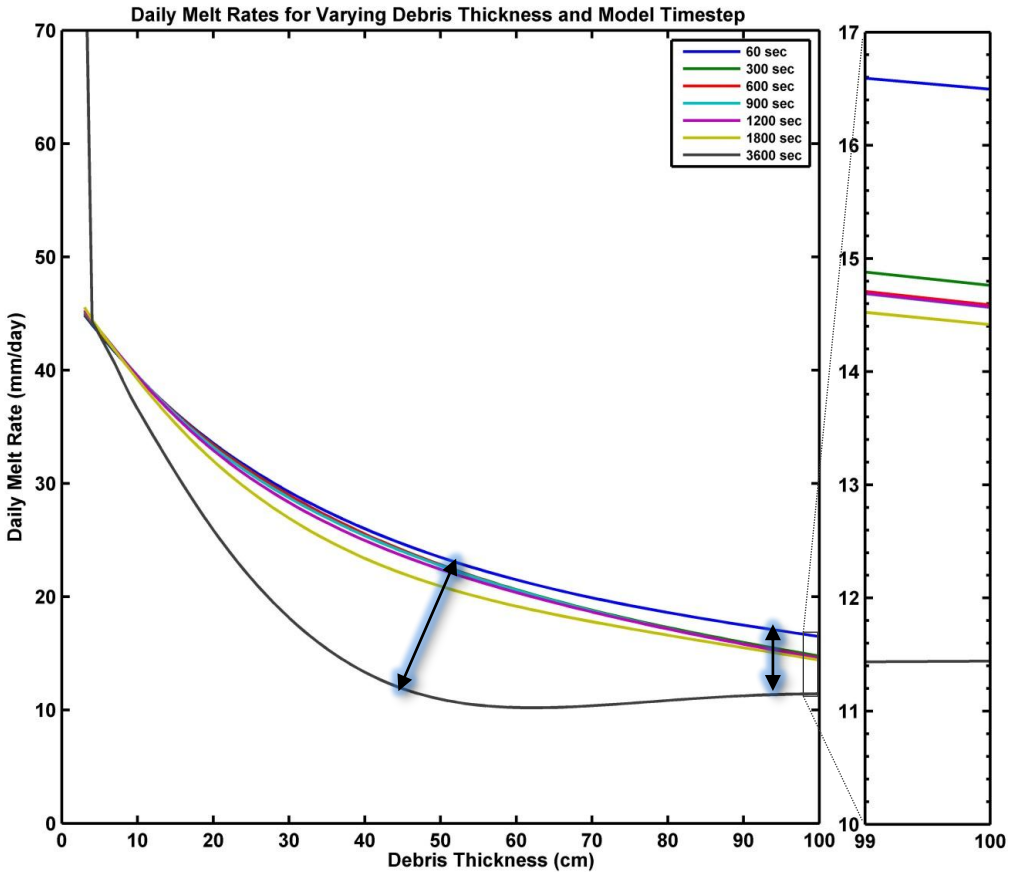

Figure 7: Synthetic Østrem curves produced from the 10th day melt using varying time steps.

The truncation error in Figure 7 clearly has a large effect on the 3600sec run yet it appears to re-converge with the other runs after an early divergence. The zoom in on the last cm of the x axis shows that for every timestep the overall error when $\Delta z \rightarrow .001$m is still between 2-5mm/day.

Daily Melt Rate vs. Shortwave Amplitude

The model has clearly shown good results in response to changes in Δz andΔt, so next a test to see how the surface energy input affected the 10th day daily melt rate. Common sense would dictate that a change in the surface energy flux will cause a proportional change in the daily melt rate.

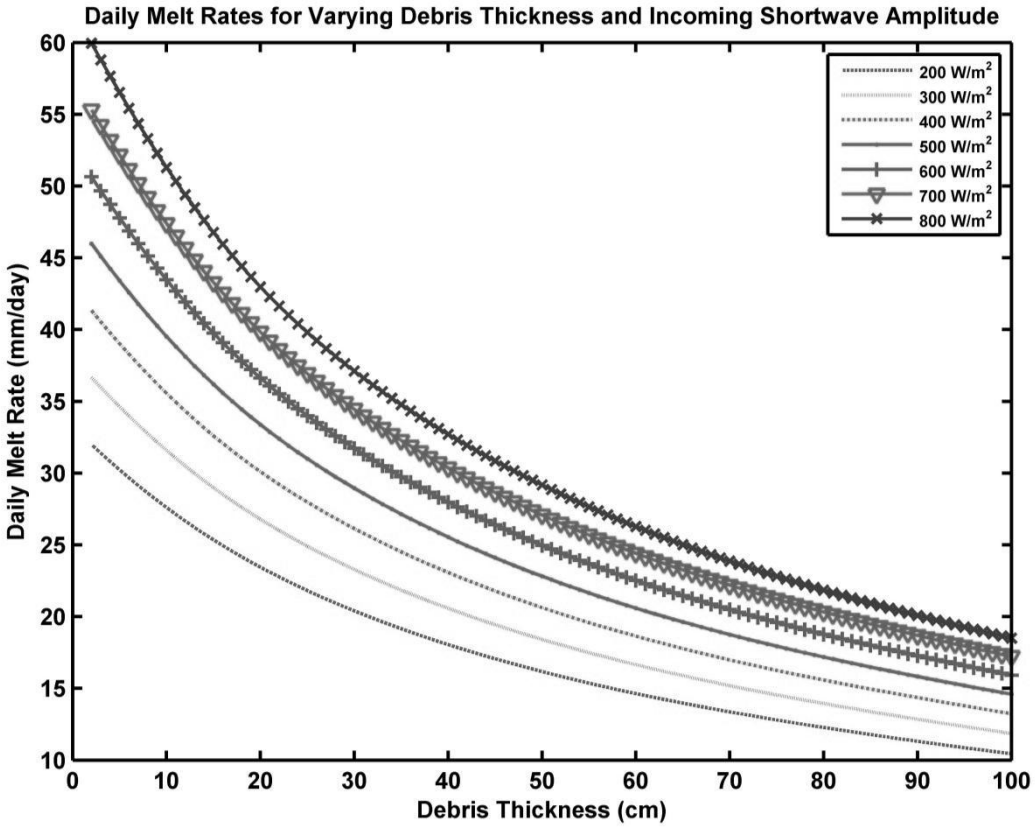

Figure 8: Variation of synthetic 10th day Østrem curves with varying shortwave amplitude.

Using a constant Δt of 60sec Figure 8 shows a clear relationship between the daily melt rate and shortwave amplitude in that an increase in the $Q_s\downarrow$ results in an increase in the daily melt rate.

It's important to note that while the curves in Figure 7 and Figure 8 are referred to as "Synthetic Østrem Curves" in fact they lack the unique Østrem feature of the increase in melt and subsequent decrease as the debris thickness approaches the "critical thickness. This distinct graphical feature is not present most likely because in the model a specific value for α of .18 is given even for very thin debris or also it may be due to the resolution of the mesh (i.e. $\Delta z \sim= 0.01m$).

5 Experimental Model Runs

To improve the already fast model performance, a graphic user interface (GUI) has been built which enables the user to alter run parameters in an interactive environment and outputs the data into individual plots and/or text flies. Doing this allows the computer to keep the data stored in global memory thereby increasing the speed at which it runs and making visualization much easier. Tests were performed to note the changes in heat flux due to altering parameters and also to see if it was possible to recreate the results of Reznichenko et al. (2010).

5.1 MODEL.m GUI

The use of a GUI allows for quick model adjustment and rapid visual analysis of individual runs. The GUI is composed of multiple parameter entry boxes and three axes for plots. Pressing the run button activates the model and then when the model is finished it sends the results back to the GUI and the axes automatically update. Doing this saves the user time in the sense that they would not have to plot all the data separately and can simply print the screen to capture the results.

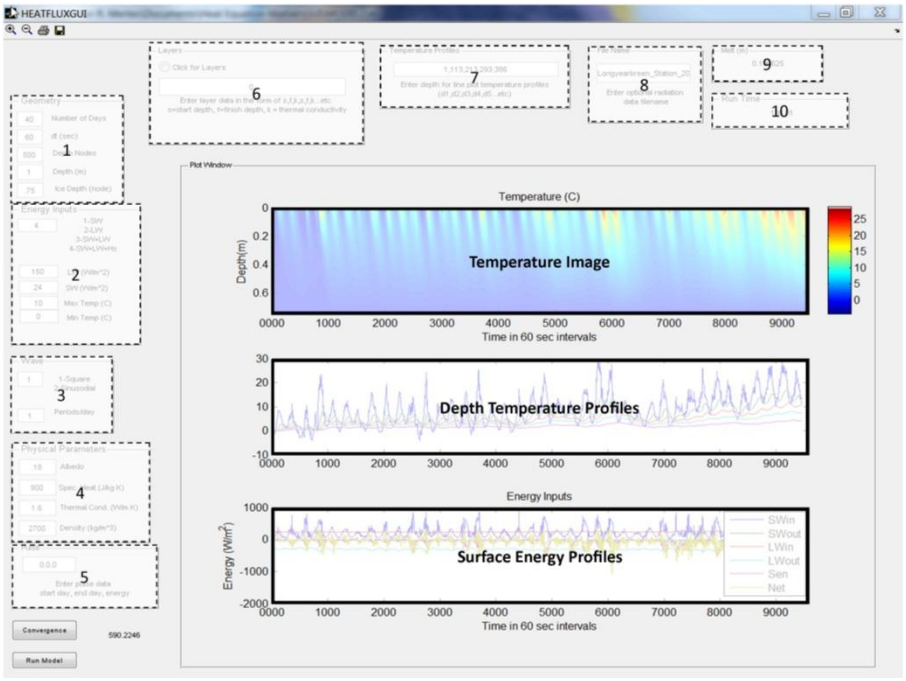

Figure 9: GUI for MODEL.m with labeled data entry locations.

The GUI parameter entry areas are seen in Figure 9, along with the three axes for plotting data. Descriptions of each are listed in Table 3 below.

Table 3: List of GUI user input boxes and a description of each.

Name	Description
1. Geometry	Used for setting up the finite mesh with entry of Days, time step, #depth nodes, total depth and ice depth
2. Energy Inputs	Choice of which heat flux sources to use along with Q_t and Q_s amplitude and temperature range (when running synthetic data)
3. Wave Form	Choice of Square or Sinusoidal wave and period specification.
4. Physical Parameters	Albedo, Specific Heat, Thermal Conductivity and Density
5. Pulse	Options for inducing a "pulse" of energy during the model run.
6. Layers	Allows for the addition of multiple layers with varying physical parameters
7. Temperature Profiles	User specification of which depth temperature profiles to plot in axes #2
8. Filename	For runs with field data specify the file name to read (i.e. *.txt)
9. Melt	Calculated melt result
10. Runtime	Total elapsed time for model to finish
11. Axes 1	Color image plot of temperature at depth vs. time
12. Axes 2	Plot of the user specified depth temperature profiles
13. Axes 3	Plot of the energy inputs vs. time

5.2 Temperature Profiles

Along with the main GUI interface window, after each model run a separate window opens with two more plots of the daily average temperature image and a line plot of the temperature profiles. Visualizing these data allows the user to see how the daily internal temperature changes with time and depth.

Numerous scientists have tested or adapted the methods of Nakawo and Young (1981) using the daily average thermal gradient to calculate melt below debris (Conway and Rasmussen 2000, Han et al. 2006, Nicholson and Benn 2006) . This method rests on the assumption that the average daily thermal gradient is linear or that the debris is in a steady state of heat flux. Results from both a steady diurnal cycle of heat input (using square waves and sinusoidal waves) and field data show that this assumption holds true for the synthetic data, however, when using field data, the daily temperature profiles are found to fluctuate away from linearity quite frequently throughout a time period.

The results of a 10 day run with both field and synthetic data can be seen below in Figure 10 and Figure 11 respectively. The model has been used to visually analyze how the daily average thermal gradient changes in response to varying debris thicknesses and when the steady diurnal cycle is interrupted by an energy pulse, simulating unstable atmospheric conditions. By determine where, and under what conditions, the daily average linear thermal gradient remains constant allows for the determination of any limitations that exist.

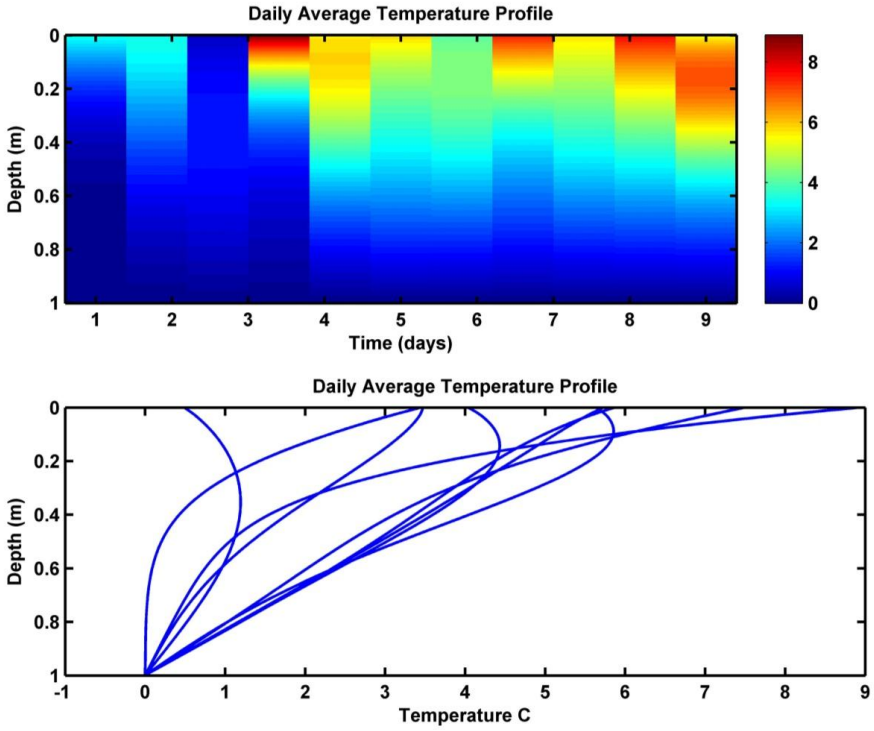

Figure 10: Daily average temperature profiles from field data for 10 days.

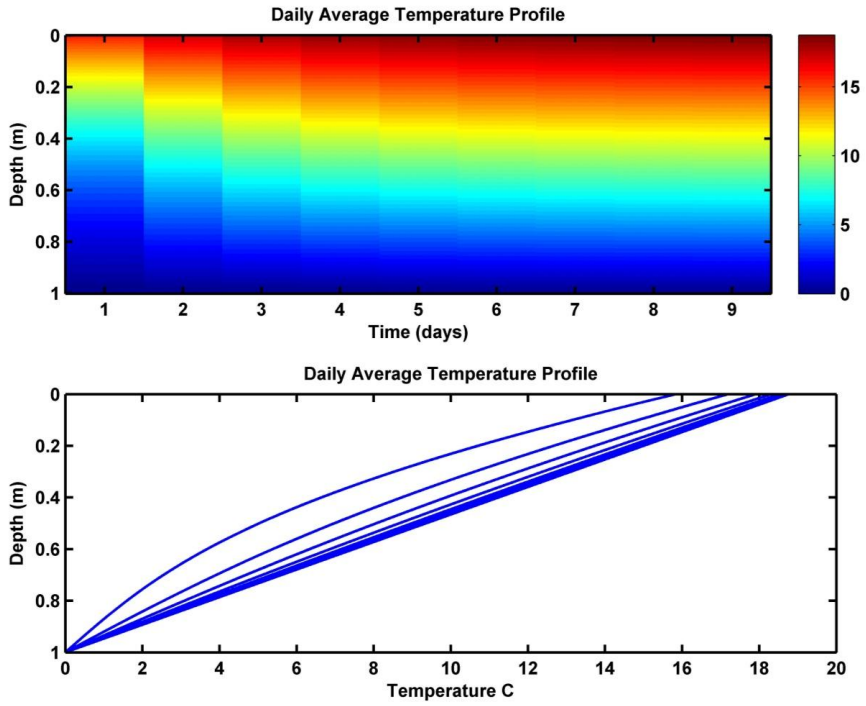

Figure 11: Daily average temperature profiles from synthetic data for 10 days.

Clearly under steady cycle condition the average daily thermal gradient will become close to constant over time. In Figure 11 the temperature profiles merge to be constant within almost the first 5 days of the 10 day run. At this point the thermal gradient is linear and equal to the

slope of the temperature profile line. In Figure 10 however, due to the fluctuating surface energy conditions the daily temperature profiles are constantly changing and the change to a more quadratic gradient is due to heat waves propagating downward through the debris.

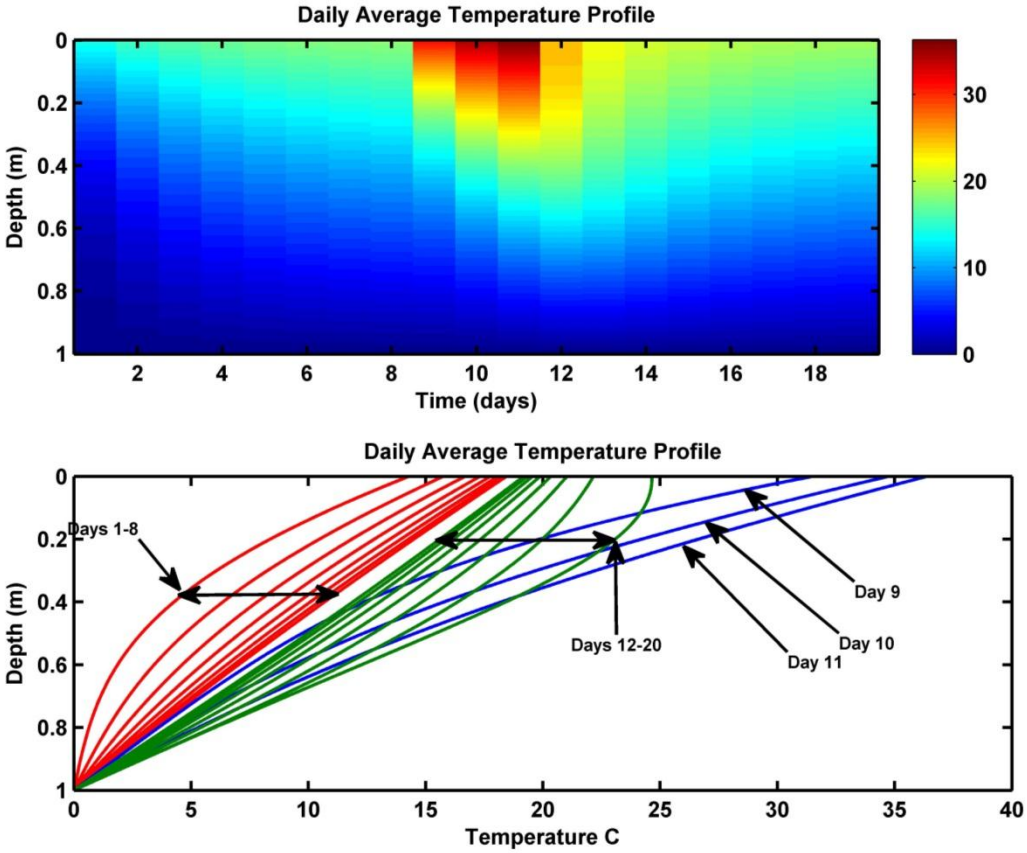

Figure 12: Daily average temperature profiles for a 20 day period with a heat pulse from 9-11th day through debris of 1m thickness. The red lines are the days up to the pulse and the green lines are the day after the pulse (blue lines).

With the addition of the pulse option in the model (#5 Figure 9) it was possible to run a longer simulation, allowing the debris to get to a steady state with a linear temperature profile (constant thermal gradient with depth) and then upset the steady state by applying an extra pulse of heat over a certain time period. Figure 12 above shows a 20 day synthetic run where from day 9-11 an extra pulse of 300 W/m^2 is added to the surface flux. As can be seen in the bottom plot, the daily average temperature profiles became almost linear within the first few days. Once the system was stable the pulse was added and on that day the internal temperatures jumped up by almost 20°C around the surface. By the 11th day the system began to relax back but took almost 4 days longer to settle back to steady state conditions.

The rate at which the system settles back to steady state is dependent on the debris thickness. If the debris layer is thinner the heat has less distance to travel, both into and out of the system and the thermal gradient becomes higher. If the debris thickness is reduced from 1m (as in the figure above) to 0.3m we can visually see the difference in the system.

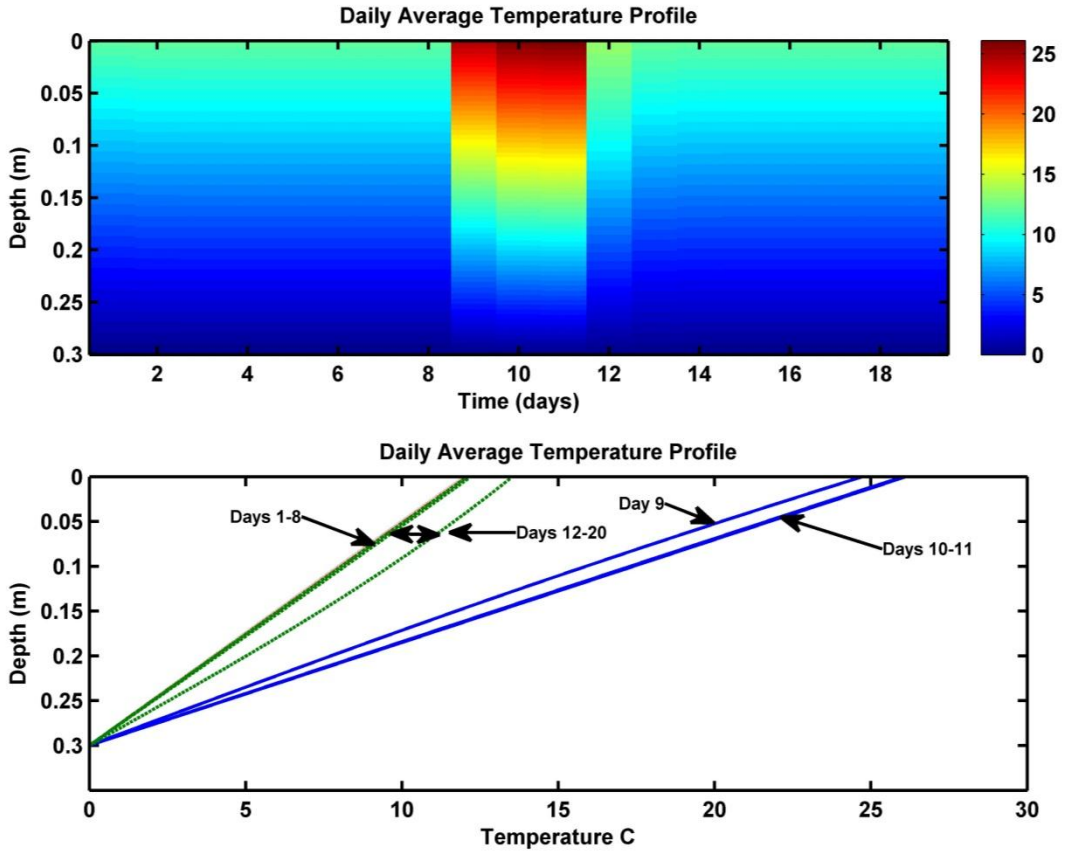

Figure 13: Daily average temperature profiles for a 20 day period with a heat pulse from 9-11th day through debris of 0.3m thickness. The red lines are the days up to the pulse and the green lines are the day after the pulse (blue lines).

The temperature in the thinner debris layer of Figure 13 goes to a steady state within the first day and remains there until the pulse is added. Unlike the 1m debris layer, however, the temperature here returns to steady state almost within the 3 days of the pulse. Also to be noted is the linearity of the profiles even when perturbed showing the average daily thermal gradient at thinner debris remains close to constant. Only day 11 shows any sign of non-linearity, yet it is still not too curved. Assuming a constant thermal gradient on a debris layer of this thickness would most likely produce very reasonable results when modeling.

On the other hand, if the debris layer thickens to 2m the effects are the opposite. The thinner the debris the more constant the daily thermal gradient remains. As the thickness increases, the heat waves have more to travel through and because of this they cannot enter and leave the layer as quickly, thereby causing the daily average thermal gradient to become more quadratic and curved.

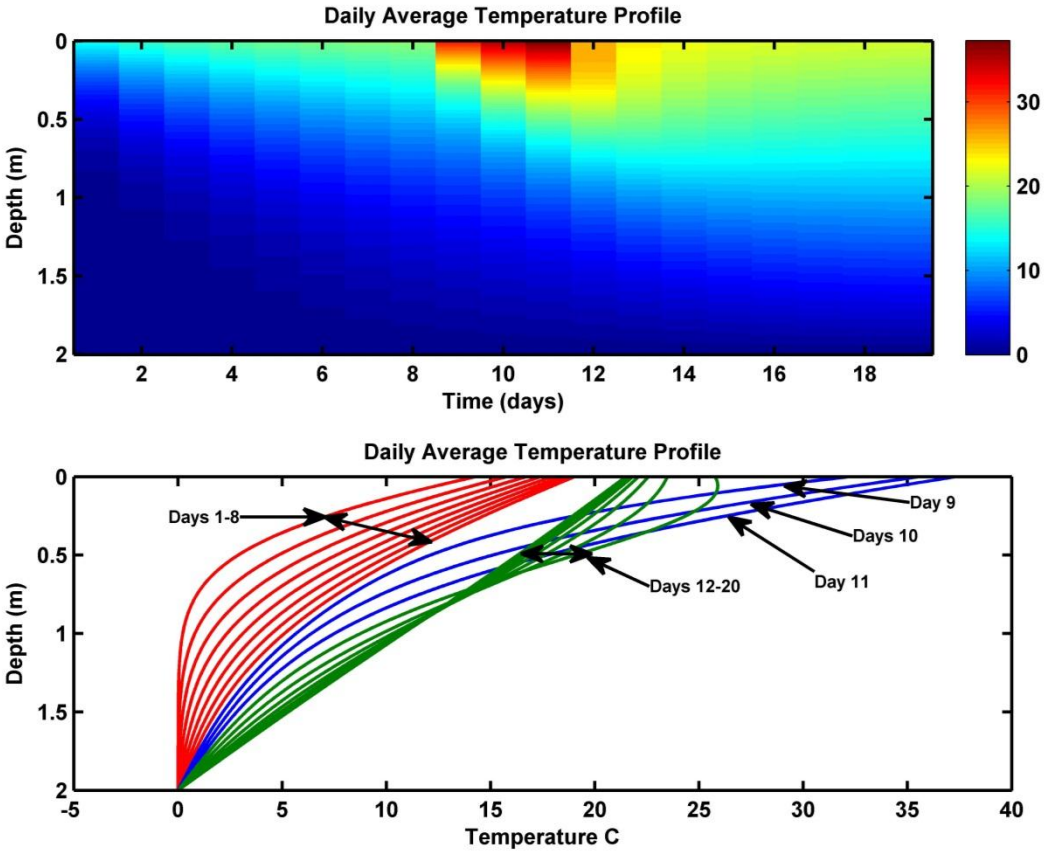

Figure 14: Daily average temperature profiles for a 20 day period with a heat pulse from 9-11th day through debris of 2m thickness. The red lines are the days up to the pulse and the green lines are the day after the pulse (blue lines).

Even within the first 8 days, a system of 2m debris thickness (Figure 14) is unable to get to steady state. The thermal gradients are approaching constant yet once the pulse is added to the system it begins stabilizing all over again and within the remaining 8 days still does not get back to a constant value.

5.3 Replication of Reznichenko et al. 2010

The laboratory experiment conducted by Reznichenko et al. (2010) consisted of measuring the melt from a block of ice under clean ice conditions and also under varying debris thicknesses (i.e. 10,50,90,130 mm). The melt was measured for steady state energy input, by constant heating of the surface, and diurnal conditions, replicated by 12hrs of heating and 12hrs of cooling with the heating being done through the use of two light bulbs (150W LW bulb, 24W SW bulb). During the cooling period the blocks of ice were placed into a freezer, away from the light source. The blocks of ice used measured 450 x 350 x 260 mm^3. The heat flux at the surface was measured using heat flux plates connected to a computer for data recording. The experimental setup can be seen in Figure 15 below.

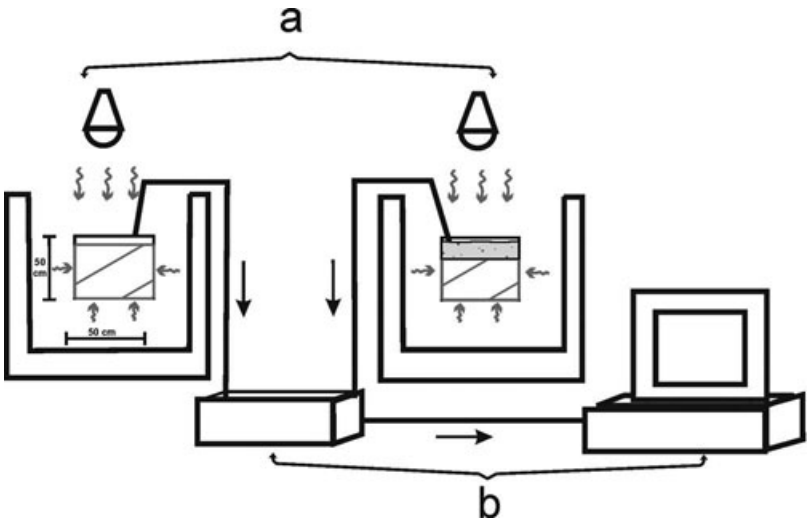

Figure 15: Laboratory setup of Reznichenko et al. sub-debris melt experiment (Reznichenko et al. 2010).

5.3.1 Calculated Melt

Based on the laboratory details presented in Reznichenko et al. (2010) the model was set up using the same incoming radiations, 150 $\left(\frac{W}{m^2}\right)$ LW, 24 $\left(\frac{W}{m^2}\right)$ SW and ambient air temperatures. Though they did not record the air temperature in their laboratory, it is possible to extract it from the data on heat flux and temperature within the block of ice. Based on these data an air temperature range of 10 °C to -2 °C has been used.

It is important to note, that based on their experimental setup, Figure 15, it appears as though they were allowing the ice/debris block to be heated and cooled from all sides. While this has not been verified yet, it may explain some differences in results. In one of their figures, they

plot the temperature vs. time for different depths. Their plot shows a slow increase in temperature for the first six hours during the warming period and then a plateau for the next six hours of warming, and then there is a sharp decrease in temperature, almost instantly, when they begin the cooling period. Using the model of this study it was impossible to replicate this form for the debris thicknesses used (i.e. 30mm, 60mm). In fact, to get a form that appears similar to theirs the debris thickness had to be set closer to 0.10m, and even then it was not possible to reproduce the extreme drop during the cooling period.

Keeping this in mind, the first experimental run of the model was to try and match the melt produced over the course of a 16 day period for 4 different thicknesses (10, 50,90,130mm) using the previously mentioned surface parameters. This run was done using the square wave diurnal cycle with a 50% duty cycle, producing 12hrs warming, 12hrs cooling.

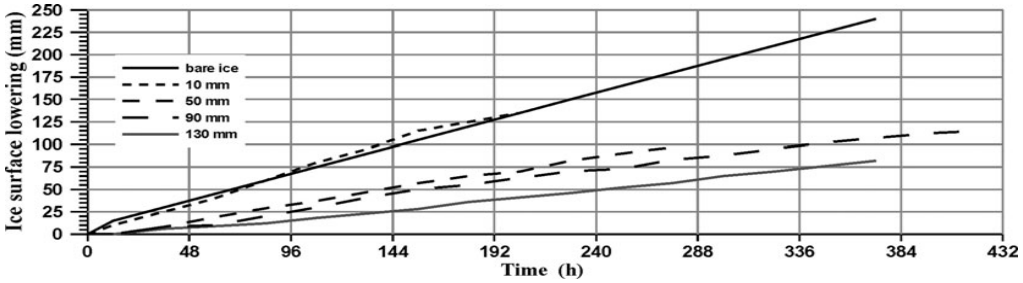

Figure 16: Cumulative melt vs. varying debris thicknesses from Reznichenko et al. 2010

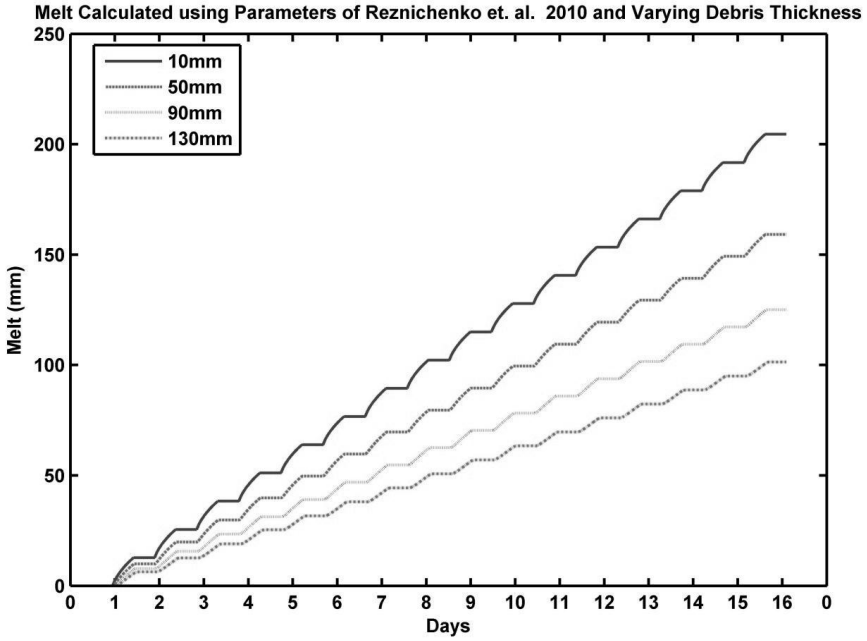

Figure 17: Cumulative melt obtained from model using parameters of Reznichenko et al. 2010.

The results obtained using the debris layers seem to fit quite well aside from the notable stepping shape of the modeled results which is a signature of the diurnal cycle and the warming and cooling periods. The modeled run used a timestep of one minute whereas the laboratory experiment sampled the data every 10 minutes. It's highly unlikely that, over a 24hr period, the stepping feature of the melt line would not be recorded.

Aside from this small difference, the model results, when compared to the actual laboratory results (interpreted from Reznichenko et al. 2010, Figure 15) show very good correlation with the laboratory results as seen in Figure 18 below.

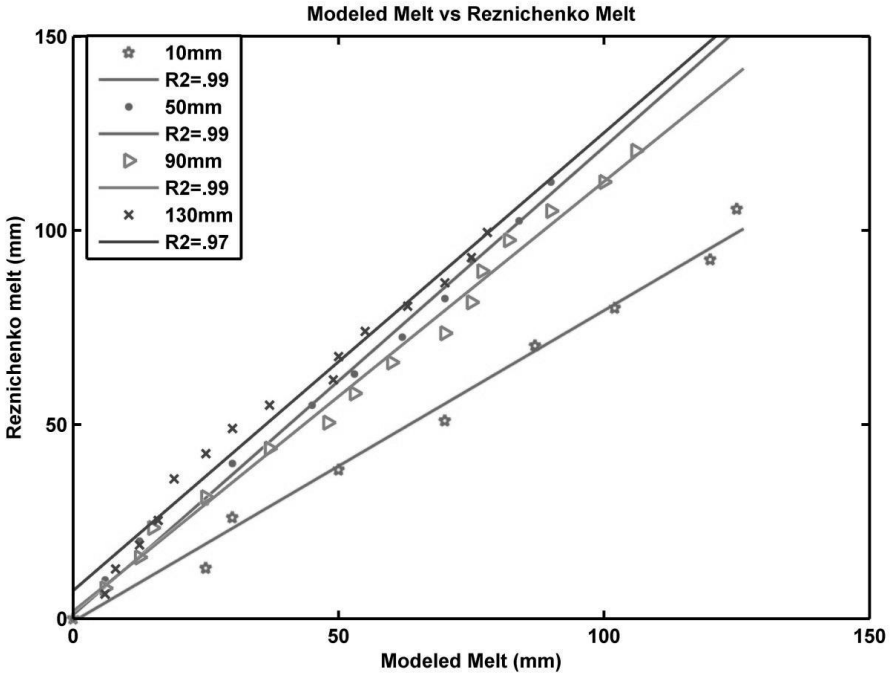

Figure 18: Laboratory results vs. Modeled Results. For all runs of varying debris thickness the R^2 values are above 0.97.

5.3.2 Effects of Varying Diurnal Cycle

Two of the main conclusions from the Reznichenko et al. (2010) study were that the atmospheric characteristics that have the most effect on the magnitude of melt are the amplitude and length of the diurnal cycle. In section 4.3.2 the model was run to tests if it could accurately reproduce the physical heat flow in a debris layer. In Figure 8 melt rates were calculated for varying shortwave mean value. It should come as no surprise that increasing the

mean value of the incoming radiation will increase the melt. However, it is also of interest to study the relationship between the amplitude and different debris thicknesses to determine how the heat lag within the debris changes when more or less heat is available at the surface.

For the next model run a melt period of 10 days was used while varying the debris thickness from 0.1m to 3m. The input net heat flux was set to 365 $\left(\frac{W}{m^2}\right)$. The amplitude was varied from $\pm 10\ to\ \pm 50\left(\frac{W}{m^2}\right)$. No noticeable change in daily melt rate was noted from this model run. The daily mean was increased to 415 $\left(\frac{W}{m^2}\right)$ and again no substantial change in daily melt rate was recorded. Based on these results there appears to be no connection with the diurnal amplitude and the amount of melt. As long as the mean value remains relatively constant the energy received at the surface during the heating part of the day is fairly equally matched by the energy transmitted during the cooling part of the day the net change in internal heat storage should remain constant, thereby causing no change to the daily melt.

6 Application of Model to Longyearbreen

For the last part of this study the model was used to calculate the melt produced during the 2010 melt season on Longyearbreen. The model has so far been able to produce results that match the expected results and has also shown limitations that have been overcome by selecting the right input parameters. It is important to test whether or not the model can reproduce the debris internal temperatures and calculate a modeled melt for the melt season. The model is then taken one step further and used to generate an Østrem for Longyearbreen based on the whole melt season. This is also done using the linear thermal gradient method as well (both average daily and full). Finally a comparison is made with curves created using smaller periods from throughout the season to determine what differences may arise.

6.1 Study Area

The study area (Figure 19) is located outside the town of Longyearbyen in the central area of the island of Spitsbergen, the largest of the Svalbard Archipelago (74°-81°N, 10°-35°E) (Spitsbergen Treaty, 1920). The climate of Svalbard is a combination of maritime and arctic climates due mainly to the position of Svalbard relative to the northern end of the North Atlantic Current. Moisture from the north and south in combination with the N-NW polar air masses brings high amounts of precipitation. The amount of annual precipitation on Svalbard decreases towards the center of the island (Humlum 2002). This is opposite to the glacier equilibrium line altitudes (ELA) which increases towards the center regions of Svalbard. The combination of these two gradients leads to a distribution

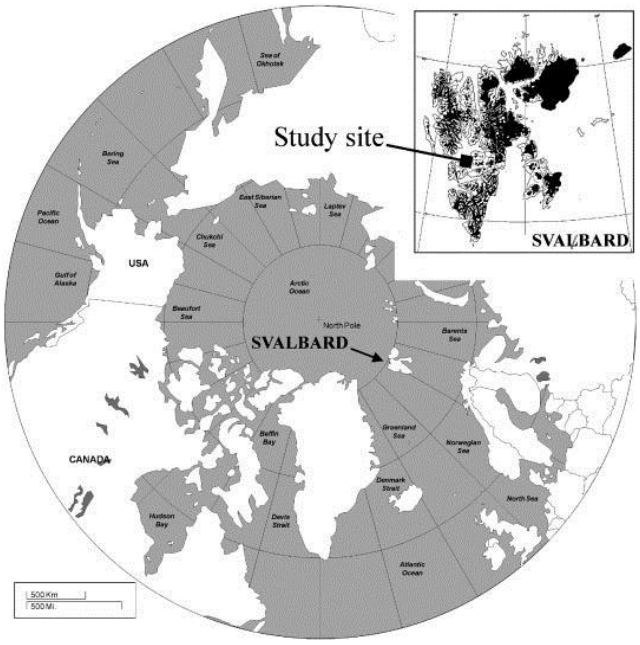

Figure 19: Study area overview (Humlum et al. 2005).

of glaciers mostly on the coastlines with some glaciers in the central regions at higher altitudes. The total glacier coverage on Svalbard has been estimated at roughly 60% and most glaciers fall into the classification of polythermal, or containing both cold ice and ice near the pressure melting point (Hagen et al. 2003b).

6.1.1 Svalbard Climate

The mean annual air temperature (MAAT) of Svalbard has been calculated at -5.2°C (aver. 1975-2000) with the warmest month being July (6.2°C) and the coldest month being February (-15.2°C). During the spring months (April-May) the weather tends to be dryer whereas during the early fall (August-September) the weather is much more humid. At the Svalbard Lufthavn (28m a.s.l.), located just outside Longyearbyen, annual precipitation has been calculated at 188mm (averaged from 1976-2010) (eKlima.met.no 2011). The wind directions are dominated by a NNW-SSE pattern (Humlum 2002), perpendicular to the Longyeardalen axis, and are the reason for the annual buildup of cornices along the upper valley walls. The snowfall that does occur on the higher plateaus is redistributed by the strong winds and deposited along the cliff edges. These cornices and other snowpack phenomena can be partially linked to the development of debris layers on glaciers in the area.

The entire area of Svalbard is underlain by permafrost. The permafrost thickness ranges from <100m in the lowlands and up to 450-600m in the mountains and plateaus (Isaksen et al. 2000, Humlum et al. 2003). The areas that are non-glaciated are therefore undergoing many different periglacial processes throughout the year (frost shattering, solifluction, creep).

6.1.2 Longyearbreen

Longyearbreen (Figure 20) is located 2.5km outside of Longyearbyen to the SW. It is flanked by high valley walls along the NW and SE sides. The surrounding geologic makeup consists of two late cretaceous sedimentary formations, Helvetiafjellet Fm. (Terrestrial SS, coal and Sh) and Carolinefjellet Fm. (Marine Sh and SS), overlain by the early Tertiary, slightly dipping, Firkanten Fm. (SS and Silt) (Harland 1998).

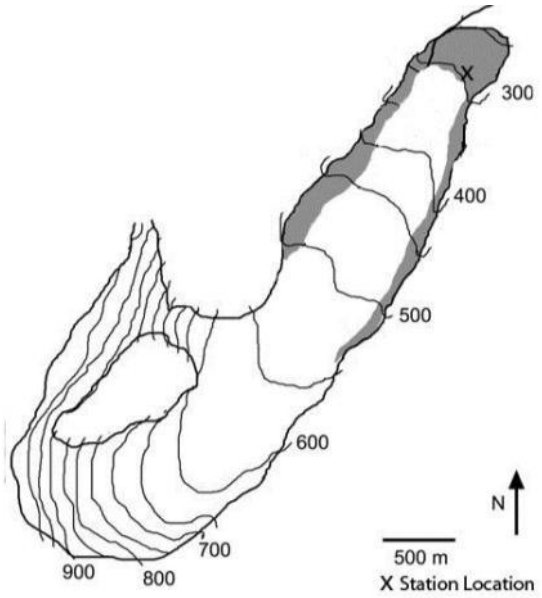

Figure 20: Longyearbreen topographic map with station location denoted by "x"(adapted from Gulley et al. (2009)).

The mountain to the NW (Nordenskiöldtoppen) rises to a height of 1050m, creating a large area for weak snow layers to build up. Along the SE side there is a flat plateau (Sarkofagen) separating Longyearbreen from the neighboring glacier Larsbreen which also develops some smaller cornices and snowfields. It's quite normal during the mid to late spring to notice numerous avalanche fans coming down from both valley walls. In fact some of these fans travel almost completely across the glacier bringing with them debris from the hillsides. Some of this debris has accumulated on Longyearbreen in the terminus region along with melt out debris. The thickness of this debris can range anywhere from .5-1.5m in thickness and be made of mostly large angular clast in a sandy matrix (Etzelmüller et al. 2000).

Data presented in Jania and Hagen (1996) gives Longyearbreen an area of 4km^2 based on work done in the mid 1970's. This same work also calculated a mean annual specific mass balance of -.55 $\frac{m\ w.e.}{yr}$. More recent measurements have calculated a width of 520m and an area of 2.53km^2 based on 1990 aerial imagery and subsequent high resolution DEM (Etzelmüller et al. 2000). Humlum et al. (2005) gave an area of 3.2 km^2. In a recent communiqué with some

of the authors it appears the most likely reason for the difference is due to the inclusion/exclusion of snowfields on the upper cirque valley walls.

Radio echo sounding profiles performed by Etzelmüller et al. (2000) showed the temperature of Longyearbreen to be below the pressure melting point. However, in the upper region, along the headwall of Nordenskiöldtoppen, there was found to be a thin layer of temperate ice, attributed to possible superimposed ice, therefore putting Longyearbreen into the "C" type polythermal glacier in the Blatter and Hutter (1991) polythermal classification. Thus any movement of the glacier comes from internal ice creep as opposed to basal sliding.

6.2 Data Collection

6.2.1 Station Installation

The weather station used for this study consists of two primary data collections units. The first being the ONSET Hobo 3m weather station and the second being the 5 Tinytag ground thermistors used to monitor the ground temperature changes at depth. The specifications of each sensor can be seen in Table 4 below.

Table 4: A Table of technical specifications for all of the weather station sensors and debris thermistors.

HOBO	Measurement Range	Accuracy	Operating Range	Resolution
Wind Speed Combo (S-WCA-M003)	0-44 m/s	±0.5m/s to ±4% in 30-44 m/s wind	-40° to 75°C	0.38 m/s
Wind Direction Sensor (S-WCA-M003)	0-358 degrees	±5 degrees	-40° to 75°C	1.4 Degrees
Wind Speed Sensor (S-WSA-M003)	0-45 m/s	±1.1m/s	-40° to 75°C	0.38 m/s
Pyranometer (S-LIB-M003)	0-1280 W/m^2	±10 W/m^2	-40° to 75°C	1.25 W/m^2
Temperature (S-THB-M00x)	-40° to 75°C	±0.2°C	-40° to 75°C	0.02°C @ 25°C
Relative Humidity (S-THB-M00x)	0-100%	±2.5 to ±3.5%	-40° to 75°C	0.1% @ 25°C
TINY TAG				
External Temperature Sensor (TGP-4020)	-40° to 125°C	0.25° to 0.5°C	-40° to 85°C	0.02°C
Thermistor Probe (PB-5002-1M5)	-40° to 125°C	0.2° to 0.3°C	-40° to 85°C	
(ONSET 2001-2010, 2008-2010b, 2008-2010a, GEMINI 2009b, 2009a, ONSET 2010)				

Both units were installed at the same location, just down glacier from the clean ice/debris-covered ice interface. The debris layer here is known to be of a thickness greater than .5m and is made of large angular clasts in a coarse-fine matrix.

This purpose of the station was to monitor the incoming heat sources and flux through the debris layer to the ice contact. The station was therefore erected on 22/05/2010 before the melt season began and taken down on 15/09/2010 just after the fall freeze began. During the excavation for the installation of the ground thermistors, frozen interstitial water and some segregated ice forms were noted, showing that the time of installation the ground was still frozen.

Due to time restraints and man power the hole that was dug for the ground thermistors was limited to roughly 56cm and 5 thermistors were installed at depths of <1, 14, 28, 42, 56 cm. The <1cm thermistor represents the field surface temperature (i.e. only shielded by a very thin layer of debris). The thermistors were installed horizontally into the debris layer and the hole was then carefully filled in, making sure not to disturb their positioning. The data loggers, which remained on the ground surface, were hidden within a cairn built out of rocks.

Figure 21: Installing debris layer thermistors (above). After final adjustments of weather station (below) (Photos by J. Mertes).

The atmospheric data collection station used for this study was an ONSET 3m Hobo weather station. The station was equipped with 2 temperature/relative humidity sensors (1.5m-3.1m), two solar radiation sensors (incoming 3.1m/outgoing 2.7m), one wind speed sensor (1.5m) and one dual wind speed/wind direction sensor (3.1m). The station was erected nearby to the

ground sensors in a position that would cast the least amount of shadow onto the ground surface and was stabilized from the wind by rock piles on each of the tripod legs (Figure 21).

6.2.2 Station Performance and Data

During the course of the data collection period the station was monitored frequently by researchers at UNIS. Data were offloaded on 12/07/2010 and 15/09/2010. On 12/07 the station appeared to be in sound condition. The level of the terrain had not undergone any extreme vertical changes and the station was still relatively level. The upper anemometer however had been damaged during a wind storm. The wind vane had come loose and broken the mounting bracket. It was then decided to leave it up yet remove the vain. Therefore from 07/12-09/15 no wind direction data were recorded.

The ground temperature thermistors were offloaded on the same dates as the station above. The only noticeable problem was discovered during removal of the thermistors from the ground. The total distance between thermistor sensors had changed slightly from the freeze thaw cycles encountered during the study period. It is most likely that the interstitial ice which had melted allowed for settlement of the debris layer and most likely through constant freeze thaw cycles these thermistors were moved from their original positions.

After analyzing the thermistor data, it appeared that there was a period from 07/07-07/12 where the surface thermistor stopped recording data. Likewise from 07/12-08/23 and again from 08/28-09/15 the thermistor at 14cm failed to record data, so for comparisons of modeled surface temperatures and actual surface temperatures, only the first 40 days have been used.

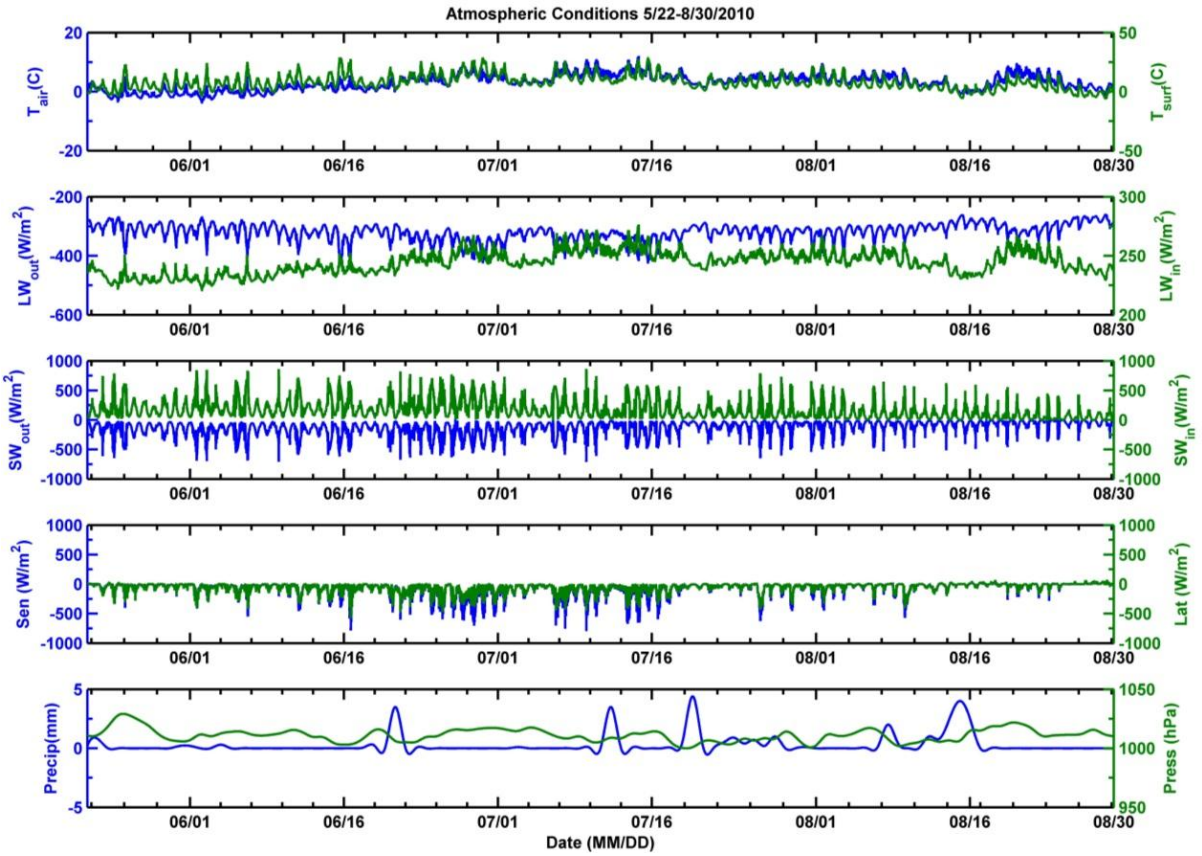

Figure 22: Atmospheric data recorded from the HOBO weather station. The bottom graph is data interpolated from the Svalbard Lufthavn (eKlima.met.no 2011).

Table 5: Summary of the recorded atmospheric data statistics.

	T_{air}	T_{surf}	LW_{out}	LW_{in}	SW_{out}	SW_{in}	Sen	Lat	Precip	Press
Min	-3.9	-6.0	-425	220	-710	16	-794	-572	0	999
Max	12.1	29.1	-259	276	-13	866	60	74	4	1029
Ave	3.1	7.9	-319	244	-136	165	-72	-59	0.3	1011

Weather conditions were fairly stable during the data collection period. The precipitation events occur when the air temperature at the site is close to zero degrees and the incoming shortwave radiation is lessened so it can be assumed that these events contributed snow to the surface which most likely melted quickly. The pressure has been calculated from the Svalbard Lufthavn weather station and adjusted for altitude. Table 5 above gives the basic statistics of

the atmospheric data set. Though the precipitation graph does show values slightly below zero, these are due to the interpolation method used and disregarded as zero.

6.3 Modeling

Running the model with the field data collected during the melt season allowed not only for testing of the performance when using real data but also to test methods used in other studies such as calculating physical properties of the debris layer from the field data, testing the limitations of the frequently used daily average linear thermal gradient method of melt calculations (Nakawo and Takahashi 1982, Nicholson 2004, Han et al. 2006, Nicholson and Benn 2006), calculating melt using atmospheric parameters compared to melt calculated from the surface temperature (Han et al. 2006) and testing the validity of calculating Østrem curves from short periods of time during the melt season.

6.3.1 Zero Degree Isotherm

To determine the 0° isotherm, linear fits were applied to the debris daily average vertical temperature profile for every timestep (every 15min). The y-intercept of these fits is a good estimate of the depth of the 0° isotherm. The model was also run using atmospheric data and a debris thickness of 2m to see if it is possible to calculate this depth without debris temperature data. The results of these calculations can be seen in Figure 23 below.

The calculated isotherm shows an extreme jump from 0.3m to 0.5m within the first 3-4 days. This sudden drop may be due to the readjustment of the debris layer to the surroundings after being dug up and exposed to the higher air temperatures. After this initial drop, the isotherm seems stable and slowly drops to about 0.7m over the next month. This slow increase from ~0.5m to ~0.7m is most likely due to the heat being absorbed by the interstitial ice as latent heat. From the end of June through the beginning of September it fluctuates around 0.7m and then slowly begins to climb at the end of the season.

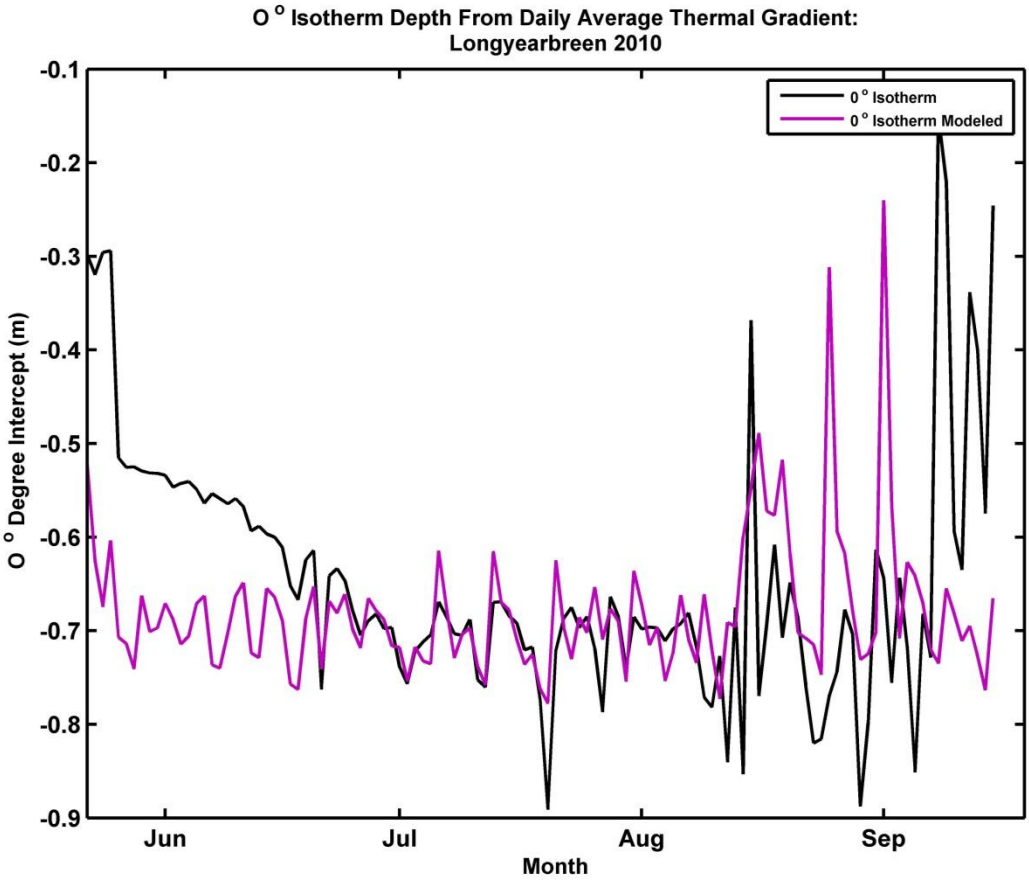

Figure 23: 0° isotherm calculated from thermistor data and from the model.

When using the modeled data the same trend is seen, however the initial drop in the beginning is not near as prominent. In fact the drop may be attributed to the same phenomena as that of starting with a debris temperature profile that is constant with depth. The model does take a couple of days to overcome the initial boundary condition of a constant temperature profile at 0°. This has been seen in both the synthetic data runs and now here. After the model has moved the system into a realistic state, the isotherm again fluctuates around the 0.7m depth for the whole of the season. The slow increase in depth is not found when using the modeled data as there is no inclusion of interstitial ice and therefore the heat wave is able to travel all the way through the debris layer.

The large spikes shown in both the modeled and the real data are most likely due to the reverse of heat flow as the surface temperatures begin to have large fluctuations. Looking at the temperature image in Figure 24 below, multiple cold waves can be seen propagating downward from the surface after mid-August and through to mid-September. These spikes, as

well as the smaller ones seen throughout the melt season represent waves from longer periods off heating or cooling. It's not unreasonable to still calculate a mean 0° depth as the mean of these lines, as the temperatures at the ice interface can, and will, fluctuate above and below freezing. The model however does not allow for excess cooling of the ice interface or for the refreezing as mentioned earlier.

6.3.2 Thermal Conductivity & Diffusivity

Following the methods of Conway and Rasmussen (2000) the debris thermal conductivity has been calculated by solving for k using Equations 4.4 and 4.5.

$$k = \rho c_s \left(\frac{\frac{\partial T}{\partial t}}{\frac{\partial^2 T}{\partial z^2}} \right) \qquad 6.1.$$

After a comparison of the modeled temperature output and the field data over the first 40days it was decided to run the model using the depths of the actual thermistors as depth nodes so it would be possible to model the debris temperature for the whole melt season.

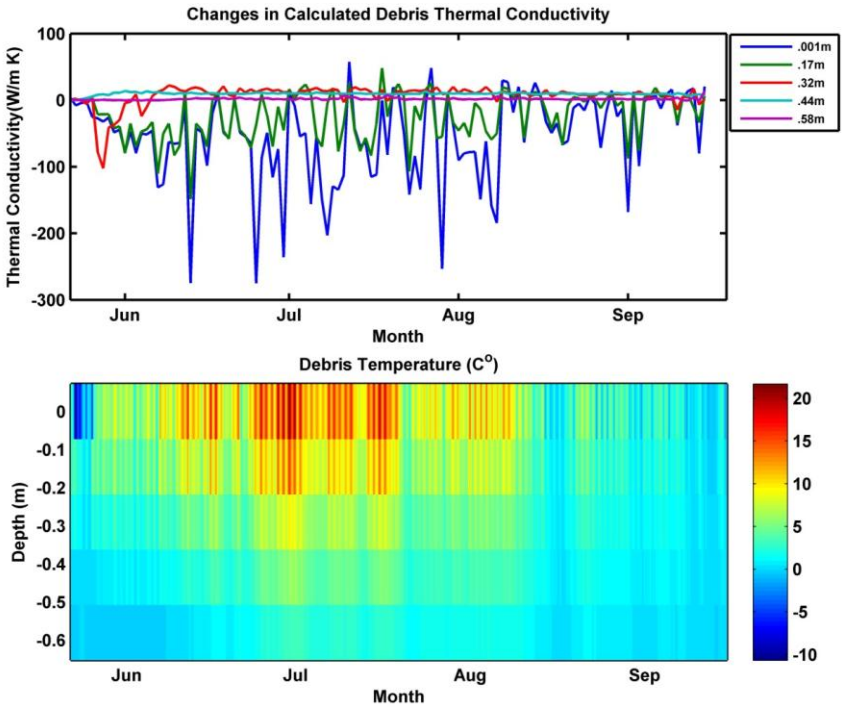

Figure 24: Variation in debris thermal conductivity for depth of thermistors (above). Coarse modeled temperature profile for the whole melt season (below).

The calculated thermal conductivities varied greatly for each depth. The two uppermost values (.001m and .17m) fluctuate greatly from 57to -274 $\frac{W}{mK}$ and 48 to -148 $\frac{W}{mK}$ respectively. Based on the data presented in Figure 22, there is no direct correlation between these peaks and, say for example, rain events. When compared to the bottom image in Figure 24 one may notice a similarity between the peak occurrences and the extreme warming events. Interstitial ice, melting and percolating further down may be the cause of this. However at 0.32m these variations are not present yet the average k value for the melt season at this depth is 1.6 $\frac{W}{mK}$. This value does agree with the value for k found by Nicholson and Benn (2006) on Larsbreen, one valley away.

6.3.3 Modeled Melt

Melt calculations were made using either the atmospheric data or the recorded surface temperature. Using the recorded surface temperature as the forcing for the model assumes that the temperature is a direct reflection of the heat exchange at the surface and can thereby be used as a "net" energy value.

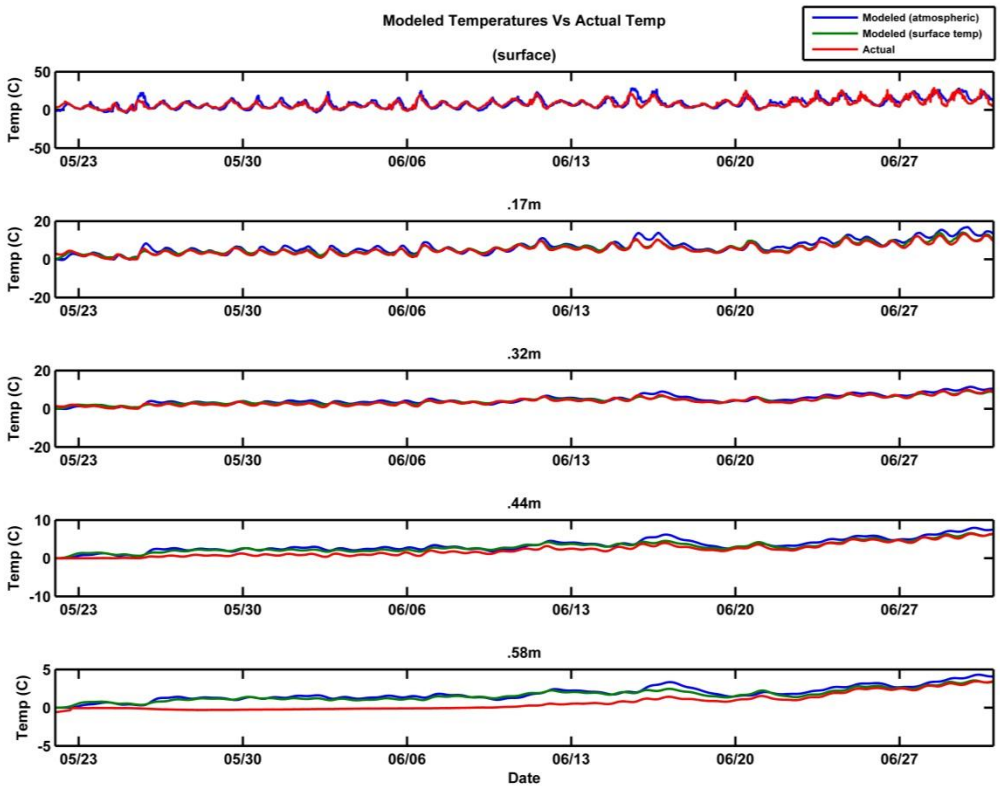

Figure 25: Comparison of calculated debris temperatures with actual temperatures.

The initial results when comparing the modeled temperatures with the actual temperature recorded by the debris thermistors show a better correlation when forced with the actual surface temperature. In Figure 25 above, both runs fit very well with the actual temperature data, however at most depths the melt using the atmospheric data forcing, overestimates the debris temperatures. The temperatures calculated from forcing the model with the actual surface temperature match quite well up until the 0.44m depth, at which point it begins to overestimate as well.

A careful examination of Figure 25 shows that at the 0.58m depth, during the first 3 weeks the debris temperature moved from subzero to zero and then stayed at zero until increasing around 06/10/2010. During excavation and placement of the thermistors, it was noted that the debris contained interstitial ice and was quite well held together. Perhaps this flat line is due to the heat wave being absorbed by the ice until it began to melt.

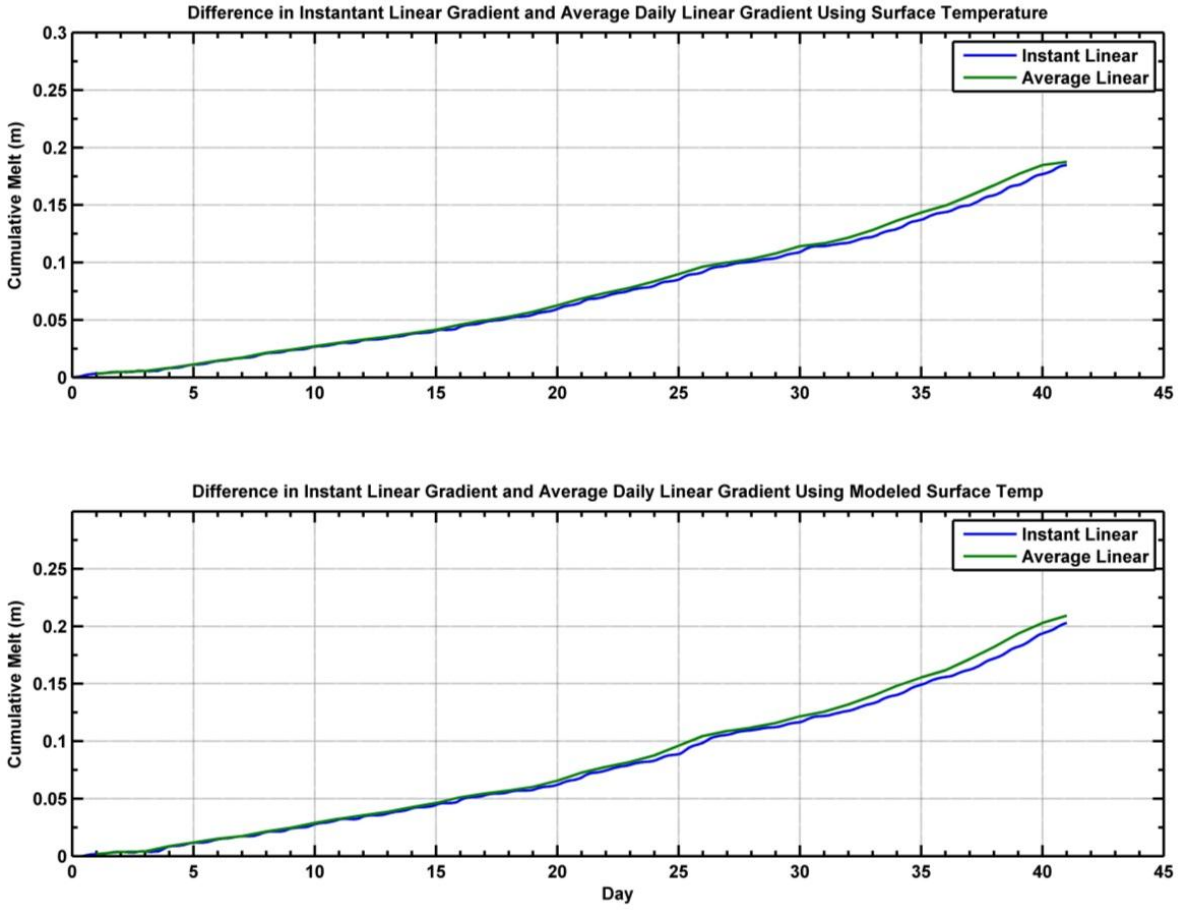

Figure 26: Melt difference between the instant linear thermal gradient and average daily linear thermal gradient. Using surface temperature as a forcing (above). Using the atmospheric data as a forcing (below).

In Figure 26 above, a comparison of the cumulative melt with time was made using the method described in Equation 4.1 using both the average daily temperature and the instantaneous temperature. This was done twice, once using the modeled surface temperature and once using the recorded surface temperatures. The calculated total melt for 40 days from both tests varies by only 0.03cm. Clearly either method can be used but since it is sometimes difficult to get all of the atmospheric data and can cost quite a bit of money, it might be beneficial to just set out surface temperature sensors in multiple locations and model with their data.

Using the atmospheric parameters for the whole melt season (100 days) it was next possible to compare the melt using the daily average linear thermal gradient method, the instantaneous linear thermal gradient method and the actual modeled melt.

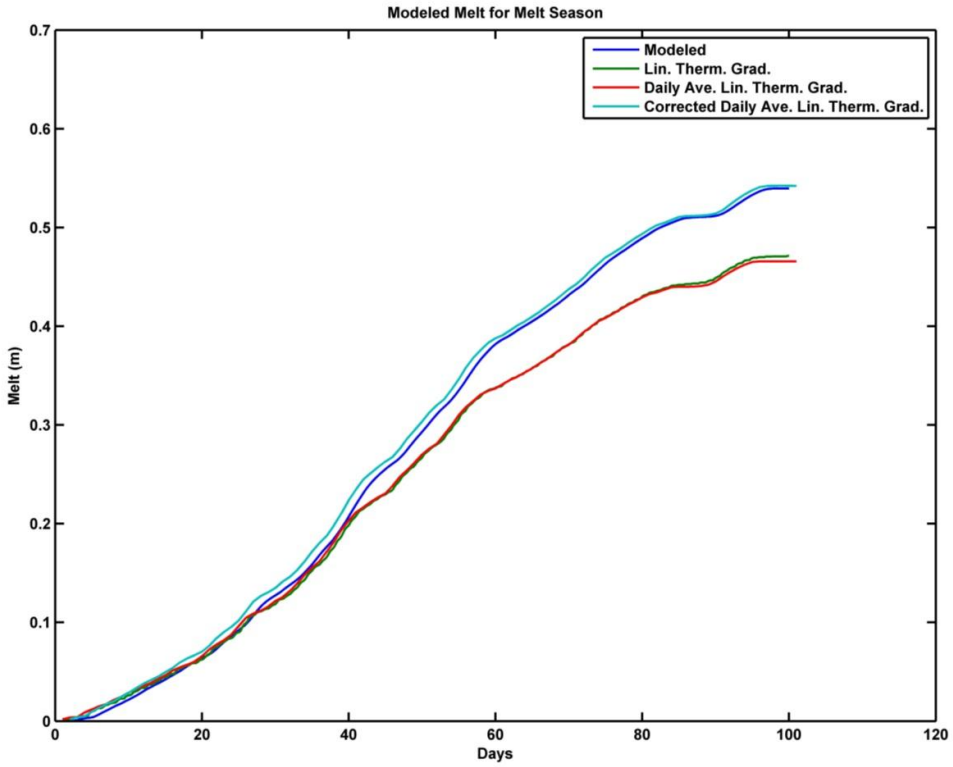

Figure 27: Comparison of melt for the whole melt season using the average linear thermal gradient method, the linear thermal gradient and the actual modeled melt.

In Figure 27 above, the results from the three different methods are shown. A method has been developed to calculate the heat flux difference with time between the actual modeled and daily average linear thermal gradients by using the following equations.

$$\left(\frac{\overline{\frac{\partial T_{norm}}{\partial z}}}{day}\right) - \left(\frac{\overline{\frac{\partial T_{line}}{\partial z}}}{day}\right) = \Delta\left(\frac{\overline{\frac{\partial T}{\partial z}}}{day}\right) \qquad 6.2.$$

Multiplying the RHS of Equation 6.2 by the debris thermal conductivity the average daily heat difference is found.

$$\Delta k\left(\frac{\overline{\frac{\partial T}{\partial z}}}{day}\right) = \Delta\left(\frac{\overline{Q_m}}{day}\right) \qquad 6.3.$$

Plugging the RHS of Equation 6.3 into Equation 4.22 for Q_m the daily average melt difference is found.

$$\left(\frac{\Delta\left(\overline{\frac{Q_m}{day}}\right)}{\rho_i L f_i}\right)(8.64\ x\ 10^6) = \Delta Melt \qquad 6.4.$$

The RHS of Equation 6.2 was correlated to the average surface temperature and a linear relationship was found such that the melt difference is dependent on the previous day's average surface temperature. When correlated to the average daily surface temperatures an R^2 of 0.5 was found when correlating with the same day and an R^2 of 0.9 was found when comparing to the previous day. So by using the linear equation found,

$$M(n) = \left(\frac{8.64\ x\ 10^6 k}{\rho_i L f_i}\right)(.1822\ T_s(n-1) + .2415) \qquad 6.5.$$

The results of using this approach to correct the error associated with using the average daily linear thermal gradient method can be seen in Figure 26 as the light blue line fitted against the dark blue line. The R^2 when correlating these two lines is .9.

6.3.4 Østrem Curve for Longyearbreen

After verification of the models performance and stability it was next used to create an Østrem curve for Longyearbreen. The model was implemented with an iterative script that calculated the cumulative melt for the whole melt season under differing debris thicknesses. This was done for all three methods; modeled, linear thermal gradient and average daily linear thermal gradient, dividing by the number of days (100) in the melt season gives a very accurate Østrem curve.

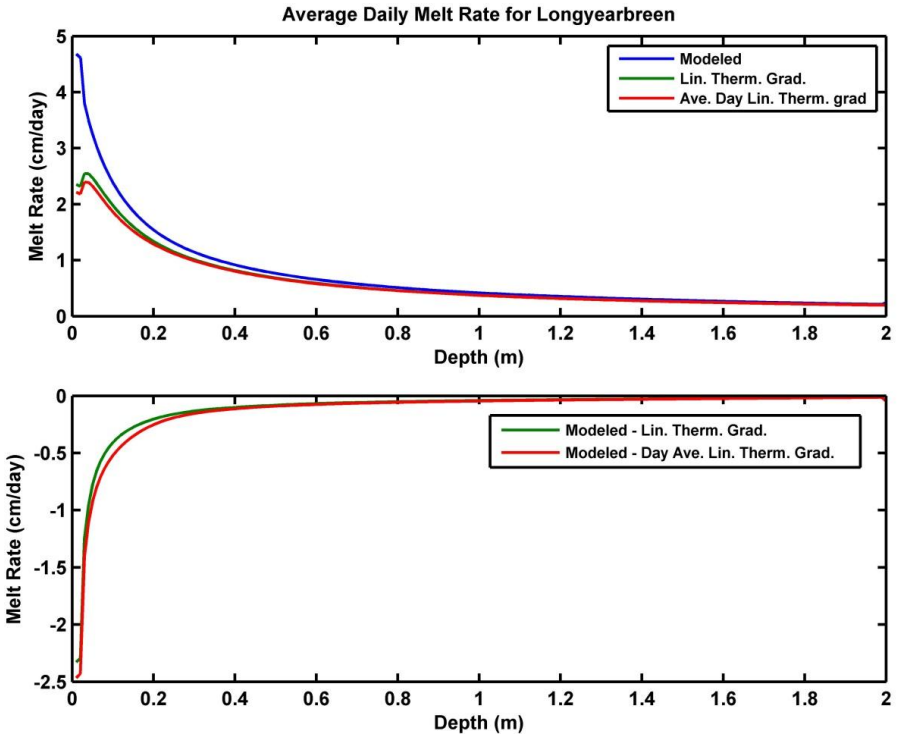

Figure 28: Østrem curve from averaging 100 days of melt for Longyearbreen (above). Differences between modeled melt and using linear thermal gradient methods (below).

In Figure 28 above, the three Østrem curves are plotted along with the differences between the linear thermal gradient methods and the modeled method. The largest differences occur within a debris thickness of <=0.4m. After 0.4m the differences slowly converge to zero. The linear thermal gradient method approaches zero slightly faster that the daily average linear thermal gradient method.

One of the largest problems with using an Østrem curve as a specific descriptor for a glacier is that most published Østrem curves have been calculated from a very short period of time during the melt season. If the period of study is done too early or too late in the melt season the Østrem curve will give values lower than the actual full melt season melt rate. If the period of study is done during the peak of the melt season the curves will give an overestimation of the melt rate, when compared to the whole season. Many scientists do attempt to collect data during the peak melt season. Table 6 below gives examples of specific studies and their observation periods. Kirkbride and Warren (1999) do mention that their measurements may not be indicative of the total seasons melt rate. For their study they attempted to extrapolate temperature data but by doing this it's more probable that the melt rate error would just grow.

Table 6: Observation periods for studies of previous sub-debris melt.

(Hagg et al. 2008)	(Kirkbride and Warren 1999)	(Mihalcea et al. 2006)	(Mihalcea et al. 2008)	(Nicholson and Benn 2006)	(Østrem 1959)	(Reid and Brock 2010)
07/30-08/10 2005	"late autumn"	07/04-07/14 2004	07/01 – 07/15 2004	07/09-07/20 2002	07/10-08/5 1956	6/21 – 09/04 2005-2007

Individual Østrem curves were made for different periods of the melt season. Using ten day periods from 15-25 June, 10-20 July and 4-14 August, it is possible to calculate how different the curves can be depending on when the observations are made. Figure 29 shows how these Østrem curves differ from the curve calculated using the average of all daily curves. Using data from mid-June and mid-August, the results show a slight overestimate and underestimate of the melt rate, respectively. The calculations made using the data from mid-July show a drastic overestimation since the data sampling occurs during the warmest month.

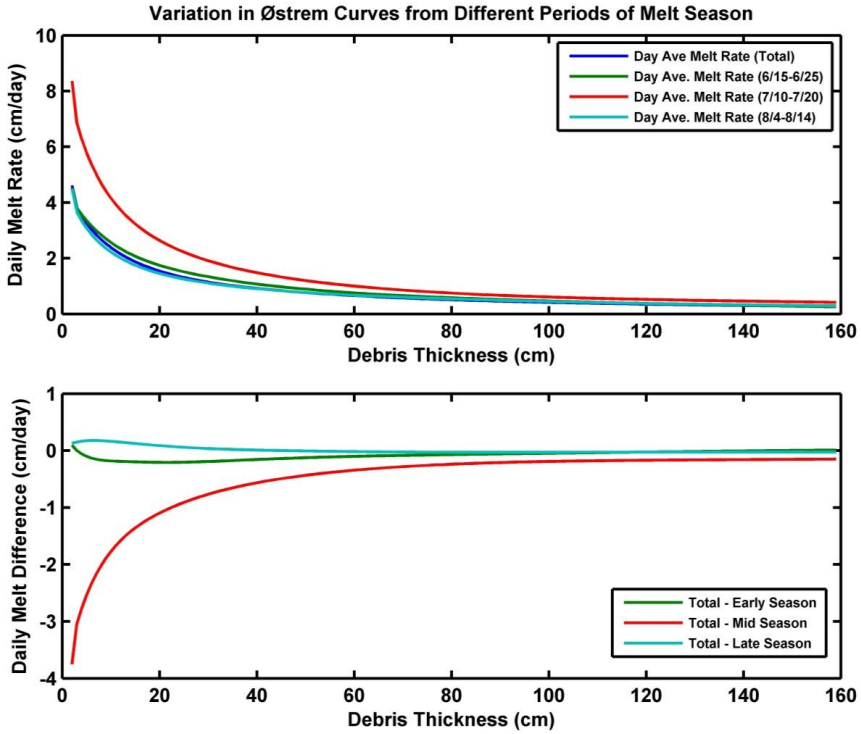

Figure 29: Modeled Østrem curves using data from 3 different time periods (above) and the differences from the actual melt (below).

Closer analysis of the daily Østrem curves revealed that only a very few matched the well-known shape that so many Østrem curves exhibit. Most of the modeled curves began with an exponential decay form but at some depth began to show a more logarithmic increase to a constant melt rate. This is obviously due to the heat waves propagating through the debris layer and causing an imbalance of heat flux at depth. If sequential curves were analyzed, for a period of changing surface temperatures, the points of zero slopes for each wave propagated deeper with each day.

7 Discussion and Conclusions

7.1 Model Performance

The model developed in this study has so far been able to function properly and shows no sign of numeric instability or dependence of results on mesh geometry. While the analysis of the truncation error propagation clearly shows a direct relationship between the magnitude of error and the size of both Δt and Δz, this error goes to zero for good combinations of both spacing values and the resulting debris layer temperatures remain similar. For the majority of the runs performed in this study, a Δt of 60s was used and a Δz ranging anywhere from 0.001m to 0.03m, and still the model performed to its expected abilities. It would be beneficial to develop both the FTCS and BTCS models and compare just how different the results may be, or if these other finite difference schemes can run with our mesh resolution.

After running numerous tests on the model, and comparing results to those of different studies, specifically Reznichenko et al. (2010), and with the data collected from Longyearbreen, it would appear that the model performs quite well. It computes results quickly, even for relatively large matrices (e.g. ~120sec for 100days at Δt=60sec) and with the implementation of the GUI it allows for quick interpretation of results in a visual environment.

7.2 Linear Gradient Method vs. Physical Model

The analysis of how the thermal gradient changes with depth has shown that when the debris layer is thin (<=0.3m) the average daily temperature profiles with depth become linear (Figure 13). When the temperature profiles are linear the thermal gradient has become constant with depth and by using the simple approach of calculating melt by using Equation 4.1, it should produce very accurate results. It is interesting to note that while the tests were run expecting a larger difference between the modeled melt and the linear method's melt to occur at depth, this was not the case. In fact the differences seen in Figure 28 occur in the upper 0.6m. This has also been verified in the Østrem curves that were created, where the

largest difference between the modeled melt and those generated using the linear thermal gradient and the average daily linear thermal gradient methods occurs within the same depth.

When using Equation 4.1on debris layers thicker than 0.3m the daily average temperature profile becomes more non-linear and a lag is also introduced in the heat wave propagation. However, when used with the field data from Longyearbreen, using the daily average surface temperature and instantaneous surface temperature, the method produced results within a few cm of the modeled melt. The accuracy of both measurements begins to become less over time. The error between the calculations compound throughout the melt season and at the end the overall melt difference is roughly 10cm. These errors can be corrected using the Equations 6.2-6.5 as proposed in this study.

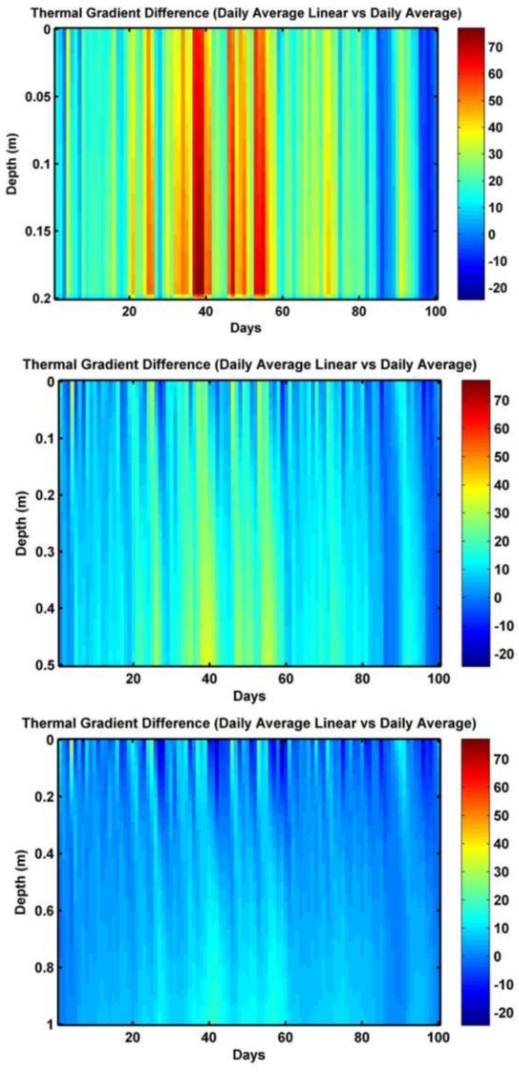

Figure 30: Changes in thermal gradient differences with depth. The colorbar on the right is in (K/m).

After visually analyzing the thermal gradient changes with depth, an inverse relationship between debris thickness and thermal gradient linearity was observed. However, for thin debris the modeled thermal gradient is not always constant. When you combine this fact with the fact that at thin debris cover the magnitude of the thermal gradient is highest as the temperature difference is calculated over a small depth. As the debris layer thickens, the magnitude of the gradient becomes less and a larger portion of the thermal gradient becomes constant, therefor the difference between the modeled thermal gradient and the linear thermal gradient decreases with increasing layer thickness as can be seen in Figure 30 above.

7.3 Replication of Reznichenko et al. 2010

When comparing the results of this study with those of Reznichenko et al 2010, there are differences that are visually apparent. Numerous questions have come up as to the actual methods used in their study. Some seem unrealistic while others are quite logical. The model was able to reproduce accurate sub-debris melt for the same time period using specific parameters that were deduced from their paper. Without knowing the k, c or ρ that were used in their study, the R^2 values for the correlation between experimental cumulative melt and modeled cumulative melt, over 16 days, were still all above .9. The physical parameters used were those from the actual runs on the field data (i.e. k=1.6, c=900 and ρ=2700).

One visually noticeable difference is the lack of a step like melt over time. While this study and the Reznichenko et al. study both can produce close to the same heat flux curves and temperature curves at different depths, the laboratory study has produced figures that raise the question of "how exactly did they heat and cool their ice?" From their diagram describing the setup, it appears as if they were heating and cooling from all sides which may explain the rapid, almost instantaneous temperature drops and increases.

7.4 Østrem Curve Analysis

The model was lastly used to generate Østrem curves for Longyearbreen using the data from the entire melt season (Figure 28 & Figure 29). The results for a debris layer thickness of 0.7m

do match with the calculated melt rate of 0.57cm/day. When multiplied by 100days this gives a cumulative melt of 0.57m which is what was calculated as the cumulative melt in Figure 27. Of great interest is why the Østrem curves generated using the linear gradient and daily average linear gradients methods both seem to have the signature Østrem rising limb whereas the modeled curve does not. Perhaps it has something to do with the physical properties of the debris and the stability of the atmospheric conditions. If the differences between the three methods decrease with increasing thickness, to the point where at a certain depth the error is due to the daily lag, perhaps the increasing limb is due to the variations which occur on a very small timescale（<1hr）which only effect the first few cm of debris. The analysis of this is beyond the scope of this study but is well worth more research.

Based on the results of calculating an Østrem curve using different periods of the melt season, it is suggested that the general practice of melt rate calculations should be done using a longer time series of surface temperature data that cover a larger portion of the melt season. This can be done by forcing the model with data from multiple surface temperature recorders. Having a longer time series only improves the accuracy of the Østrem curve for the glacier in question. If the scientific community is going to continue using these curves as way of describing glacial melt below debris they need to represent the entire melt season as large differences are apparent when using data from small time periods within the melt season. Producing Østrem curves by following this protocol would allow a better comparison of how different glaciers, in different settings respond to debris cover.

7.5 Concluding Remarks

Overall the model has performed as expected and has been able to be implemented to study not only how heat is transferred through a debris layer using a full physical model but also how this differs from the simplified linear thermal gradient method. Both methods have their limitations and both can be used in specific settings. For debris layers over 0.5m melt calculations can be made using either method, however, when the debris layer is thinner the physically based model should be used, as the linear thermal gradient method has a higher error.

7.6 Further Research

The model has been shown to be able to quickly and accurately model the flux of heat through a debris layer. Further development can be done to increase the speed by using faster coding. It may also be possible to reduce the truncation error through the method of over relaxation which results in faster convergence of values towards the true solution. Clearly for shorter time periods the model does produce accurate results as was shown when replicating the Reznichenko study. However since the truncation error does grow with time, it is crucial that the model uses a very fine mesh for longer runs.

For further work with this model it would be beneficial to gather field data on the surface lowering rate on Longyearbreen. By setting out numerous ground surface temperature sensors along with a sonic ranger, mounted onto a vertical pole that is anchored deep into the ice, it could be possible to run the model again, for another melt season and have actual surface lowering data for verification of accuracy.

Another way to move forward with this study is to measure surface temperatures using laser temperature sensors from a higher vantage point around the glacier. By marking locations on the glacier and measuring at these spots throughout the melt season it would be possible, with data on average debris thickness, to get an estimate of melt for the whole surface. To go further with this idea, one could mount a laser temperature sensor onto an automatic tripod which can be programmed to focus on certain points (much like an automatic telescope tripod) and can collect data. The biggest question is how atmospheric variability would affect these measurements (e.g. clouds, fog, snow, rain). The measurements would need to be done on clear days.

References

Andreas, E.L. 2009. A New Value of the von Kármán's Constant: Implications and Implementation. *Journal of Applied Meteorology and Climatology* 48, 923-944.

Andreassen, L.M. 1999. Compairing Traditional Mass Balance Measurements with Long-term Volume Change Extracted from Topographical Maps: A Case Study of Storbreen Glacier in Jotunheimen, Norway, for the Period 1940 - 1997. *Geogr Ann* 81A, 467-476.

Andreassen, L.M., Elvehøy, H., Kjøllmoen, B., Engeset, R.V. and Haakensen, N. 2005. Glacier Mass-balance and Length Variation in Norway. *Ann Glaciol* 42, 317-325.

Arnold, N.S., Rees, W.G., Hodson, A.J. and Kholer, J. 2006. Topographic Controls on the Surface Energy Balance of a High Arctic Valley Glacier. *J Geophys Res* 111, 15.

Benn, D.I. and Lehmkuhl, F. 2000. Mass Balance and Equilibrium-line Altitude of Glaciers in High-mountain Environments. *Quatern Int* 65/66, 15-29.

Benn, D.I., Wiseman, S. and Hands, K.A. 2001. Growth and drainage of supraglacial lakes on debrismantled Ngozumpa Glacier, Khumbu Himal, Nepal. *Journal of Glaciology* 47, 626-638.

Bindi, M., Miglietta, F. and Zipoli, G. 1992. Different Methods for Separating Diffuse and Direct Components of Solar Radiation and their Application in Crop Growth Models. *Clim Res* 2, 47-54.

Blatter, H. and Hutter, K. 1991. Polythermal Conditions in Arctic Glaciers. *J Glaciol* 37, 261-270.

Braithwaite, R. and Olesen, O.B. 1990. A Simple Energy-Balance Model to Calculate Ice Ablation at the Margin of the Greenland Ice Sheet. *J Glaciol* 36, 222-229.

Brock, B.W., Willis, I.C. and Sharp, M.J. 2006. Measurement and parameterization of aerodynamic roughness length variations at Haut Glacier d'Arolla, Switzerland. *Journal of Glaciology* 52, 281-297.

Brock, B.W., Willis, I.C., Sharp, M.J. and Arnold, N.S. 2000a. Modelling Seasonal and Spatial Variations in the Surface Energy Balance of Haut Glacier d'Arolla, Switzerland. *Ann Glaciol* 31, 53-63.

Brock, B.W., Willis, I.C., Sharp, M.J. and Arnold, N.S. 2000b. Modelling seasonal and spatial variations in the surface energy balance of Haut Glacier d'Arolla, Switzerland. *Annals of Glaciology* 31, 53-62.

Cenderelli, D.A. and Wohl, E.E. 2001. Peak discharge estimates of glacial-lake outburst floods and "normal" climatic floods in the Mount Everest region, Nepal. *Geomorphology* 40, 57-90.

Charnley, F.E. 1959. Some Observations on the Glaciers of Mt. Kenya. *J Glaciol* 3, 480-492.

Conway, H. and Rasmussen, L.A. 2000. Summer Temperature Profiles within Supraglacial Debris on Khumbu Glacier, Nepal. *Debris-Covered Glaciers*, Seattle, Washington, USA.

Crank, J. and Nicolson, P. 1947. A practical method for numerical evaluation of solutions of partial differential equations of the heat-conduction type. *Mathematical Proceedings of the Cambridge Philosophical Society* 43, 50-67.

Cuffey, K.M. and Paterson, W.S.B. 2010. *The Physics of Glaciers*. 4 ed, Amsterdam: Elsevier. XII, 650 s. pp.

Dortch, J.M., Owen, L.A., Caffee, M.W. and Kamp, U. 2011. Catastrophic partial drainage of Pangong Tso, northern India and Tibet. *Geomorphology* 125, 109-121.

eKlima.met.no. 2011. *eKlima*. Norwegian Meteorological Institute 2011 Accsessed: 4/15 2011]. Available at http://www.eklima.met.no.

Etzelmüller, B., Ødegård, R.S., Vatne, G., Mysterud, R.S., Tonning, T. and Sollid, J.L. 2000. Glacier Characteristics and Sediment Transfer System of Longyearbreen and Larsbreen, Western Spitsbergen. *Norsk Geog Tidssrk* 54, 157-168.

GEMINI. 2009a. *Gemini Data Loggers: Fast Response Thermistor Probe (PB-5002-1M5)*. *GEMINI Corp*.

GEMINI. 2009b. *Gemini Data Loggers: Tinytag Plus 2 Temperature Logger for Thermistor Probe (TGP-4020). GEMINI Corp.*

Gratton, D.J., Howarth, P.J. and Marceau, D.J. 1993. Using Landsat-5 thematic mapper and digital elevation data to determine the net radiation field of a Mountain Glacier. *Remote Sensing of Environment* 43, 315-331.

Gulley, J.D., Benn, D.I., Müller, D. and Luckman, A. 2009. A Cut-and-closure Origin for Englacial Conduits in Uncrevassed Regions of Polythermal Glaciers. *J Glaciol* 55, 66-81.

Hagen, J.O., Kohler, J., Melvold, K. and Winther, J.-G. 2003a. Glaciers in Svalbard: Mass Balance, Runoff and Freshwater Flux. *Polar Research* 22, 145-159.

Hagen, J.O. and Liestøl, O. 1990. Long-term Glacier Mass-balance Investigations in Svalbard 1950-88. *Ann Glaciol* 14, 102-107.

Hagen, J.O., Melvold, K., Eiken, T., Isaksson, E. and Lefauconnier, B. 1999. Mass Balance Methods on Kongsvegen, Svalbard. *Geogr Ann* 81A, 593-601.

Hagen, J.O., Melvold, K., Pinglot, F. and Dowdeswell, J. 2003b. On the Net Mass Balance of the Glaciers and Ice Caps in Svalbard, Norwegian Arctic. *Arc Antarct Alp Res* 35, 264-270.

Hagg, W., Mayer, C., Lambrecht, A. and Helm, A. 2008. SUB-DEBRIS MELT RATES ON SOUTHERN INYLCHEK GLACIER, CENTRAL TIAN SHAN. *Geografiska Annaler: Series A, Physical Geography* 90, 55-63.

Han, H., Ding, Y. and Liu, S. 2006. A Simple Model to Estimate Ice Ablation Under a Thick Debris Layer. *J Glaciol* 52, 528-537.

Harland, W.B. 1998. *The Geology of Svalbard.* Geological Society Memoir. 17: Geological Society of London. 529 pp.

Hay, J.E. and Fitzharris, B.B. 1988. A Comparison of the Energy-balance and Bulk-aerodynamic Approaches for Estimating Glacier Melt. *J Glaciol* 34, 145-154.

Hock, R. 2005. Glacier Melt: a Review of Processes and Their Modelling. *Prog Phys Geog* 29, 362-391.

Holmlund, P. 1987. Mass Baance of Storglaciaren During the 20th Century. *Geogr Ann* 69, 24.

Humlum, O. 2002. Modelling Late 20th-century Precipitation in Nordenskild Land, Svalbard, by Geomorphic Means. *Norsk Geog Tidssrk* 56, 96-103.

Humlum, O., Elberling, B., Hormes, A., Fjordheim, K., Hansen, O.H. and Heinemeier, J. 2005. Late-holocene Glacier Growth in Svalbard, Documented by Subglacial Relict Vegetation and Living Soil Microbes. *The Holocene* 15, 396-407.

Humlum, O., Instanes, A. and Sollid, J.L. 2003. Permafrost in Svalbard: a Review of Research History, Climatic Background and Engineering Challenges. *Polar Research* 22, 191-215.

Isaksen, K., Mühll, D.V., Gubler, H., Kohl, T. and Sollid, J.L. 2000. Ground Surface-temperature Reconstruction Based on Data from a Deep Borehole in Permafrost at Janssonhaugen, Svalbard. *Ann Glaciol* 31, 287-295.

Jania, J. and Hagen, J.O., eds 1996. *Mass Balance of Arctic Glaciers.* Report No. 5 utg, *Working Group on Arctic Glaciology*. University of Silesia: IASC.

Jansson, P. 1999. Effect of Uncertainties in Measured Variables on the Calculated Mass Balance of Storglaciaren. *Geogr Ann* 81A, 633-642.

Kaser, G., Fountain, A. and Jansson, P. 2003. *A Manual for Monitoring the Mass Balance of Mountain Glaciers.* Paris. UNESCO. 137 pp.

Keller, B. and Costa, A.M.S. 2009. A Matlab GUI for Calculating the Solar Radiation and Shading of Surfaces on the Earth. *Comput Appl Eng Educ* doi: 10.1002/cae.20301.

Kirkbride, M.P. and Warren, C.R. 1999. Tasman Glacier, New Zealand: 20th-century thinning and predicted calving retreat. *Global and Planetary Change* 22, 11-28.

Konig-Langla, G. and Augstein, E. 1994. Parameterization of the Downward Long-wave Radiation at the Earth's Surface in Polar Regions. *Meteorol Zeitschrift* N.F.3 Jg. 1994, 5.

Luthcke, S.B., Arendt, A.A., Rowlands, D.D., McCarthy, J.J. and Larsen, C.F. 2008. Recent glacier mass changes in the Gulf of Alaska region from GRACE mascon solutions. *Journal of Glaciology* 54, 767-777.

Mihalcea, C., Mayer, C., Diolaiuti, G., D'Agata, C., Smiraglia, C., Lambrecht, A., Vuillermoz, E. and Tartari, G. 2008. Spatial distribution of debris thickness and melting from remote-sensing and meteorological data, at debris-covered Baltoro glacier, Karakoram, Pakistan. *Annals of Glaciology* 48, 49-57.

Mihalcea, C., Mayer, C., Diolaiuti, G., Lambrecht, A., Smiraglia, C. and Tartari, G. 2006. Ice ablation and meteorological conditions on the debris-covered area of Baltoro glacier, Karakoram, Pakistan. *Annals of Glaciology* 43, 292-300.

Nakawo, M. and Rana, B. 1999. Estimate of Ablation Rate of Glacier Ice Under a Supraglacial Debris Layer. *Geogr Ann* 81A, 695-701.

Nakawo, M. and Takahashi, S. 1982. A Simplified Model for Estimating Glacier Ablation Under a Debris Layer. *Hydrological Aspects of Alpine and High Mountain Areas*, Exeter, UK.

Nakawo, M. and Young, G.J. 1981. Field Experiments to Determine the Effect of a Debris Layer on Ablation of Glacier Ice. *Annals of Glaciology* 2, 85-91.

Nicholson, L. 2004. *Modelling Melt Beneath Supraglacial Debris: Implications for the Climatic Response of Debris-covered Glaciers*, Department of Geography, University of St. Andrews, St. Andrews, Scotland, UK. 355.

Nicholson, L. and Benn, D.I. 2006. Calculating ice melt beneath a debris layer using meteorological data. *Journal of Glaciology* 52, 463-470.

Nuth, C., Moholdt, G., Kohler, J., Hagen, J.O. and Kääb, A. 2010. Svalbard Glacier Elevation Changes and Contribution to Sea Level Rise. *J Geophys Res* 115, 16.

Oerlemans, J. 1992. Climate Sensitivity of Glaciers in Southern Norway: Application of an Energy-Balance Model to Nigardsbreen, Hellstugubreen and Alfotbreen. *J Glaciol* 38, 223-233.

Oerlemans, J. 2010. *The Microclimate of Valley Glaciers*, Utrecht: Igitur, Utrecht Publishing & Archiving Services. 138 pp.

Oerlemans, J. and Klok, E.J. 2002. Energy Balance of a Glacier Surface: Analysis of Automatic Weather Station Data from the Morteratschgletscher, Switzerland. *Art Antarc Alp Res* 34, 477-485.

Olsson, H. and Ahlmann, H.W. 1936. Scientific Results of the Norwegian-Swedish Spitzbergen Expedition in 1934. Part VIII. *Geogr Ann* 18, 225-244.

ONSET. 2001-2010. *Silicon Pyranometer Smart Sensor (Part # S-LIB-M003)*: Onset Computer Corporation.

ONSET. 2008-2010a. *Temperature/RH Smart Sensor (S-THB-M00x)*: Onset Computer Corporation.

ONSET. 2008-2010b. *Wind Speed/Direction Smart Sensor (Part # S-WCA-M003)*: Onset Computer Corporation.

ONSET. 2010. *Wind Speed Smart Sensor (Part # S-WSA-M003)*: Onset Computer Corporation.

Østrem, G. 1959. Ice Melting Under a Thin Layer of Moraine, and the Existance of Ice Cores in Moraine Ridges. *Geogr Ann* 41, 228-230.

Parkinson, C.L. and Washington, W.M. 1979. A Large Scale Numerical model of sea ice. *J Geophys Res* 84, 26.

Parry, M.L., Canziani, O.F., Palutikof, J.P., Linden, P.J.v.d. and Hanson, C.E., eds 2007. *IPCC, Climate Change 2007: Impacts, Adaptation and Vulnerability*. Cambridge: Cambridge University Press.

Pellicciotti, F., Brock, B., Strasser, U., Burlando, P., Funk, M. and Corripio, J. 2005. An Enhanced Temperature-index Glacier Melt Model Including the Shortwave Radiation Balance: Development and Testing for Haut Glacier d'Arolla, Switzerland. *J Glaciol* 51, 573-587.

Recktenwald, G. demoCN.m. Portland. *Solve 1D heat equation with Crank-Nicolson scheme on a uniform mesh*

Recktenwald, G. 2011b. Finite-Difference Approximations to the Heat Equation.

Recktenwald, G. 2011c. Numerical Solution of Partial Differential Equations. Portland.Personal Communication

Recktenwald, G. tridiagLU.m. Portland. *Obtain the LU factorization of a tridiagonal matrix*

Recktenwald, G. tridiagLUsolve.m. Portland. *tridiagLUsolve Solve (LU)*v = d where L and U are LU factors of a tridiagonal matrix*

Reid, T.D. and Brock, B.W. 2010. An Energy-balance Model for Debris-covered Glaciers Including Heat Conduction through the Debris Layer. *J Glaciol* 56, 903-916.

Reznichenko, N., Davies, T., Shulmeister, J. and McSaveney, M. 2010. Effects of Debris on Ice-surface Melting Rates: an Experimental Study. *J Glaciol* 56, 384-394.

Rial, J.A. 2011. *Geology 15: The Dynamic Earth*. University of North Carolina at Chapel Hill 2011 Accsessed: 05/02 2011]. Available at http://www.geolab.unc.edu/classes/Geo15/G15.newest.html.

Roerink, G.J., Su, Z. and Menenti, M. 2000. S-SEBI: A simple remote sensing algorithm to estimate the surface energy balance. *Physics and Chemistry of the Earth, Part B: Hydrology, Oceans and Atmosphere* 25, 147-157.

Shroder, J., Bishop, M.P., Bulley, H.N.N., Haritasya, U.K. and Mertes, J.R. 2008. Hindu Kush & Himalayan Glacier Changes: Global Change Anomalies. *Mountains as Early Indicators of Climate Change,* 17-18 April, Padova Italy, 75-79.

Takeuchi, Y., Kayastha, R.B. and Nakawo, M. 2000. Characteristics of Ablation and Heat Balance in Debris-free and Debris-covered areas on Khumbu Glacier, Nepal Himalayas, in the Pre-monsoon Season. *Debris-Covered Glaciers (Proceedings of a Workshop)*, September 2000, Seattle, Washington, USA, 53-61.

Tangborn, W.V., Krimmel, R.M. and Meier, M.F. 1971. A Comparison of Glacier Mass Balance by Glaciological, Hydrological and Mapping Methods, South Cascade Glacier, Washington. *Snow and Ice - Symposium - Neiges et Glaces*, Moscow, 185-196.

Zakšek, K., Podobnikar, T. and Oštir, K. 2005. Solar Radiation Modelling. *Comput Geosci* 31, 233-240.